Acta Materialia 250 (2023) 118884

Contents lists available at ScienceDirect

Acta Materialia

journal homepage: www.elsevier.com/locate/actamat

Full length article

Microstructure and mechanical behavior of additively manufactured CoCrFeMnNi high-entropy alloys: Laser directed energy deposition versus powder bed fusion☆

Yanfang Liu [a,b,1], Jie Ren [b,1], Shuai Guan [b], Chenyang Li [c], Yin Zhang [d], Saideep Muskeri [e], Zhiyuan Liu [f], Dunji Yu [g], Yan Chen [g], Ke An [g], Yang Cao [a,*], Wei Liu [a], Yuntian Zhu [a,h], Wei Chen [c], Sundeep Mukherjee [e], Ting Zhu [d], Wen Chen [b,*]

[a] Nano and Heterogeneous Materials Center, School of Materials Science and Engineering, Nanjing University of Science and Technology, Nanjing, 210094, China
[b] Department of Mechanical and Industrial Engineering, University of Massachusetts, Amherst, MA 01003, USA
[c] Department of Mechanical, Materials, and Aerospace Engineering, Illinois Institute of Technology, Chicago, IL 60616, USA
[d] George W. Woodruff School of Mechanical Engineering, Georgia Institute of Technology, Atlanta, GA 30332, USA
[e] Department of Materials Science and Engineering, University of North Texas, Denton, TX 76203, USA
[f] Additive Manufacturing Institute, College of Mechatronics and Control Engineering, Shenzhen University, Shenzhen, 518060, China
[g] Neutron Scattering Division, Oak Ridge National Laboratory, Oak Ridge, TN 37831, USA
[h] Department of Materials Science and Engineering, City University of Hong Kong, Kowloon, Hong Kong, China

ARTICLE INFO

Keywords:
Additive manufacturing
High-entropy alloy
Crystallographic texture
Mechanical property
Deformation mechanism

ABSTRACT

CoCrFeMnNi high-entropy alloys (HEAs) are additively manufactured by laser directed energy deposition (L-DED) and laser powder bed fusion (L-PBF) processes. Comparative studies are conducted for the microstructures and deformation mechanisms of L-DED and L-PBF samples. In both types of samples, highly heterogeneous microstructures are formed, consisting of columnar grains, solidification cells, and dislocation networks. However, substantial differences are measured in the crystallographic texture, cell size, and elemental distribution. Deeper melt pools in the L-DED samples promote a mixed crystallographic texture of <101>/<111> as opposed to <001> along the build direction in the L-PBF samples. The <101>/<111> texture elevates the flow stresses and facilitates the activation of deformation twins in the L-DED samples. Moreover, their larger solidification cell sizes and associated chemical segregation across cell walls increase the dislocation storage capability and resistance to dislocation motion, leading to profuse planar slip bands and microbands during plastic deformation. The enhanced plastic deformation capabilities in the L-DED samples give rise to more sustained strain hardening and thus higher ductility compared to the L-PBF samples. Our work not only provides fundamental insights into the deformation mechanisms of additively manufactured HEAs, but also underscores the critical impact of processing conditions on the solidification microstructure and material design by additive manufacturing.

1. Introduction

High-entropy alloys (HEAs) represent an emerging class of alloys containing five or more elements in equimolar or near-equimolar proportions [1]. The multi-principal elements of HEAs lead to high configurational entropy and severe lattice distortion. The rise of HEAs has shifted the material design paradigm from the corners of a phase diagram to the more spacious central region, which opens up new opportunities for material development [2,3]. Although fundamental questions such as thermodynamic and kinetic origins of phase selection

☆ This manuscript has been authored by UT-Battelle, LLC, under contract DE-AC05–00OR22725 with the US Department of Energy (DOE). The US government and the publisher, by accepting the article for publication, acknowledges that the US government retains a nonexclusive, paid-up, irrevocable, worldwide license to publish or reproduce the published form of this manuscript, or allow others to do so, for US government purposes. DOE will provide public access to these results of federally sponsored research in accordance with the DOE Public Access Plan (http://energy.gov/downloads/doe-public-access-plan).

* Corresponding authors.
E-mail addresses: y.cao@njust.edu.cn (Y. Cao), wenchen@umass.edu (W. Chen).

[1] These authors contributed equally to this work.

https://doi.org/10.1016/j.actamat.2023.118884
Received 22 November 2022; Received in revised form 23 February 2023; Accepted 25 March 2023
Available online 27 March 2023

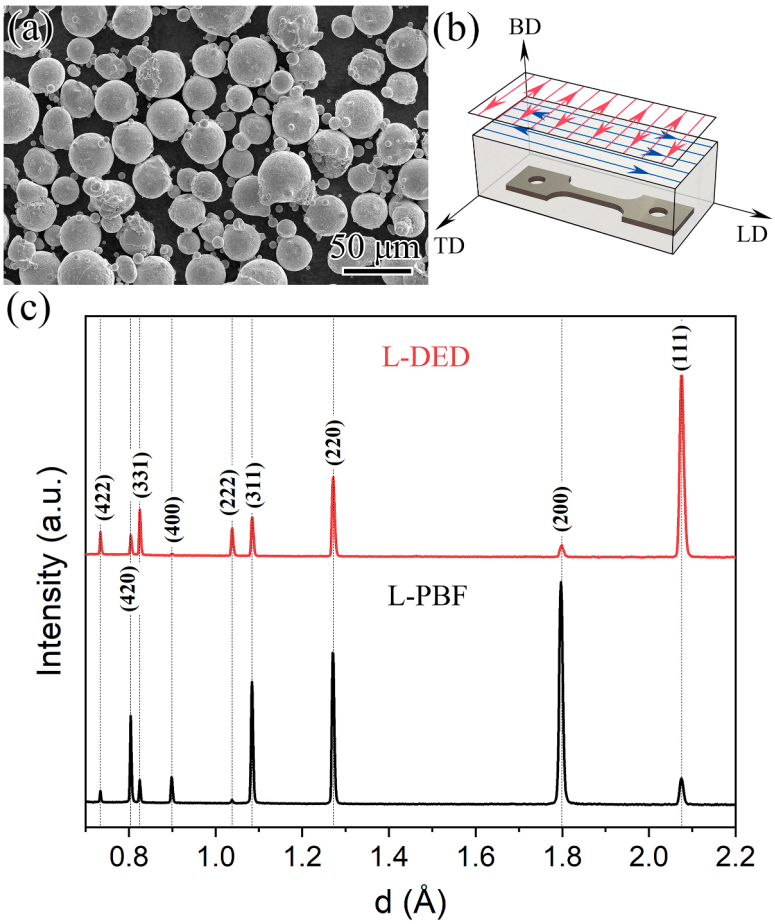

Fig. 1. CoCrFeMnNi powders, AM scan strategy, and neutron diffraction of printed samples. (a) SEM image of gas-atomized CoCrFeMnNi powders with the particle sizes in the range of 15–53 μm; (b) Schematic of the bi-directional and cross-hatched laser scan strategy. The tensile loading direction (LD) of dog-bone samples is perpendicular to the build direction (BD); (c) Neutron diffraction patterns of the L-DED and L-PBF CoCrFeMnNi samples along the BD.

remain elusive, many HEAs have shown exceptional mechanical properties, including high strength, excellent fracture toughness, and robust fatigue resistance, making them promising candidates for structural applications [4,5].

HEAs are mainly synthesized by casting to date [6]. Additive manufacturing, also called 3D printing, is a rapidly developing technology that enables direct production of geometrically complex parts. The extreme solidification conditions (e.g., large thermal gradients and high cooling rates) during additive manufacturing result in non-equilibrium microstructures that often consist of unconventional crystallographic textures, heterogeneous grain morphologies, sub-grain dislocation cells, and chemical segregation [7,8]. Interestingly, many additively manufactured (AM) metallic alloys such as stainless steels, titanium alloys, aluminum alloys, and HEAs have demonstrated superior mechanical properties that are not readily accessible by conventional processing routes [7,9-13].

To harness the combined advantages of additive manufacturing and HEAs, there is currently a critical need for the fundamental understanding of microstructure and mechanical behavior of AM HEAs [14]. This is because, on one hand, the intense laser processing, large thermal gradients, and rapid solidification result in highly heterogeneous microstructures that can greatly impact the mechanical behavior of AM materials. On the other hand, the multi-component elements in HEAs are expected to strongly influence the chemical and structural heterogeneities and accordingly the mechanical responses of AM HEAs. While additive manufacturing has received considerable attention in the past decade, the processing-structure-property relationship in AM metal alloys is not clearly understood [15]. This challenge is largely due to the variations of printing technologies as well as the enormous processing parameter space that make it possible to produce diverse microstructures and properties, even for the same alloy composition [16]. In principle, the solidification structure is governed by the shape of the melt pool and the thermal conditions at the liquid/solid interface, such as local temperature gradient (G) and solidification growth rate (R), which can vary significantly with different printing protocols [16]. For example, Supplementary Fig. S1 presents different solidification conditions and resulting mechanical properties for 316L stainless steel (SS) produced by two most common metal printing technologies, i.e., laser powder bed fusion (L-PBF) and laser directed energy deposition (L-DED) [17]. For L-DED, powders are fed and melted by a coaxial laser beam to achieve layer-by-layer deposition. For L-PBF, thin layers (30–50 μm) of powders are spread and a laser beam selectively fuses exposed regions to achieve layer-wise deposition. These two metal printing processes differ in their scan speeds and solidification rates. Supplementary Fig. S1a and b show vast differences in heat input, temperature gradient, and solidification rate between the two printing processes, resulting in several orders of magnitude variations in cooling rates (as controlled by $G{\cdot}R$) during L-PBF (10^5–10^6 K/s) and L-DED (10^3–10^4 K/s). These differences in processing conditions lead to different solidification microstructures and thus mechanical properties (Supplementary Fig. S1c). For example, metal alloys fabricated by L-PBF with higher cooling rates tend to exhibit more refined dislocation cell structures and higher strengths than those by L-DED [9,18-20].

In this work, we take the multi-component CoCrFeMnNi alloy as a model system and perform a comparative study on the microstructure, mechanical behavior, and deformation mechanism of AM HEAs

produced by L-PBF and L-DED processes. CoCrFeMnNi, first developed by Cantor et al. [1], has been widely studied due to its excellent mechanical properties at both ambient and cryogenic temperatures [21, 22]. Our work reveals distinct microstructures including melt pool geometry, crystallographic texture, and solidification cell structure in AM CoCrFeMnNi by the two different printing techniques. Through a suite of characterization tools including neutron diffraction, electron backscatter diffraction (EBSD), transmission electron microscopy (TEM), and density functional theory (DFT) calculations, we investigate the mechanistic roles of multiscale structural characteristics in plastic deformation of the two AM CoCrFeMnNi HEAs. We find that deeper melt pools in L-DED samples facilitate the formation of a mixed crystallographic texture of <101>/<111> as opposed to <001> along the build direction (BD) in L-PBF samples with shallower melt pools. The preferred texture of <101>/<111> in the L-DED samples promotes enhanced Taylor strengthening, giving yield strengths comparable to those of the L-PBF samples despite much lower cooling rates in the former case. Moreover, the <101>/<111> texture, together with larger sizes of solidification cells and stronger chemical heterogeneity across these cells in the L-DED samples, improves the dislocation accumulation capability and promotes the activation of deformation twins and microbands. These enhanced plastic deformation capabilities result in more sustained work-hardening and thus higher ductility for L-DED samples than L-PBF samples. Our findings not only provide insights into the deformation mechanisms of AM HEAs, but also shed light on the importance of tuning laser printing protocols for material design.

2. Methods

2.1. Additive manufacturing

L-DED samples were manufactured by an Optomec L-DED 450 system with a laser beam size of 400 μm. Gas-atomized CoCrFeMnNi powders with particle sizes in the range of 15–53 μm (Fig. 1a) were used. The samples were deposited onto a low-carbon steel substrate by a bi-directional and cross-hatched scan strategy, as illustrated in Fig. 1b. The processing chamber was filled with high-purity argon; the oxygen content was maintained below 10 ppm during printing. To obtain near fully-dense samples, we performed a series of control experiments by building CoCrFeMnNi cubes (8 mm × 8 mm × 8 mm) and applied a density optimization approach. With a constant hatching distance of 0.4 mm and a pre-set layer thickness of 0.25 mm, we varied the scan speed from 12.7 to 16.9 mm/s, laser power from 270 to 350 W and powder feed rate from 3 to 3.5 rpm to cover a wide range of laser energy densities. The relationship between the relative density of the L-DED CoCrFeMnNi samples and the laser energy density is shown in Supplementary Fig. S2a. The following effective processing parameters that yielded near fully-dense samples (99.85% relative density) were selected for printing large plate samples: laser power = 270 W, scan speed = 12.7 mm/s, volumetric energy density = 213 J/mm^3, and powder feed rate = 3 rpm.

L-PBF samples were manufactured by an EOS M290 system with a laser beam size of 100 μm. The same powder feedstock and scan strategy were used as in the L-DED process. A high-strength 4340 steel substrate was pre-heated to 80 °C to minimize thermal residual stresses during L-PBF. Following the same density optimization approach as for L-DED samples, L-PBF samples were printed with a constant layer thickness of 0.04 mm and a hatching distance of 0.08 mm but with varying scan speeds from 500 to 2500 mm/s and laser powers from 250 to 370 W. As shown in Supplementary Fig. S2b, near fully-dense samples (99.65% relative density) were successfully fabricated with the optimized processing condition of 300 W laser power and 1000 mm/s scan speed.

2.2. Microstructural characterization and mechanical testing

The chemical compositions of as-printed CoCrFeMnNi samples were analyzed by inductively coupled plasma mass spectroscopy (ICP-MS) for metallic elements and instrumental gas analysis (IGA) for non-metallic elements including oxygen and nitrogen. The relative densities of as-printed CoCrFeMnNi samples were measured by an AccuPyc II 1340 gas pycnometer. The phase and microstructure were studied by neutron diffraction, optical microscopy (OM), EBSD, and TEM. Samples for OM analysis were mechanically polished and etched in a solution of 50% aqua regia and 50% ethanol. Samples for neutron diffraction and EBSD studies were further polished using 1 μm diamond suspension and 50 nm alumina suspension to remove surface-strained layer. TEM samples were prepared by grinding to a thickness of 90 μm, followed by electropolishing in an electrolyte of 20% nitric acid and 80% methanol with an operating voltage of 40–50 V at a temperature of −40 °C until a central perforation was observed. EBSD analyses were performed using a Zeiss Auriga scanning electron microscope equipped with energy-dispersive X-ray spectroscopy (EDS). Step sizes of 0.05 μm, 0.2 μm and 1.5 μm were used to capture microstructures of different feature sizes during the EBSD experiments. TEM experiments were carried out on a TECNAI-G2–20-LaB_6 microscope operating at 200 kV. Neutron diffraction experiments were carried out in the VULCAN beamline - engineering materials diffractometer at the Spallation Neutron Source (SNS), Oak Ridge National Laboratory (ORNL). With a slit size of 5 mm × 3 mm, the neutron diffraction spectra were collected in a high-intensity mode with an instrument resolution of ~0.45%. Full width at half maximum (FWHM) of different diffraction peaks was extracted by the pseudo-Voigt function convoluted with back-to-back exponential single-peak fitting via the VDRIVE software [23].

Dog-bone-shaped specimens with a gauge dimension of 8 mm × 2 mm × 1 mm were cut from the built plate. Uniaxial tensile tests with the loading direction (LD) perpendicular to the build direction (BD) were conducted on an Instron 5969 universal testing machine at room temperature with a strain rate of 2×10^{-4} s^{-1}. An Instron non-contact AVE2 video extensometer with a displacement resolution of 0.5 μm was used for precise strain measurement. Before the test, the sample surfaces were polished by 1200-grit SiC paper. The tests were repeated three times for each type of AM samples to quantify the standard error bars. Stress relaxation experiments were performed at 5 interrupted strains of 1%, 2%, 5%, 10% and 15%, under a strain-control mode at room temperature. The samples were loaded to the target strains with a strain rate of 2×10^{-4} s^{-1}, followed by stress relaxation as a function of time for 50 s at different strain levels. After stress relaxation at each interrupted strain, the samples were continuously reloaded to the same stress level at the onset of the previous cycle for next relaxation. Four relaxation cycles were conducted at each strain.

Table 1
Chemical compositions of L-DED and L-PBF CoCrFeMnNi HEAs (wt.%).

	Cr	Mn	Fe	Co	Ni	O	N
L-DED	18.8	19.1	19.8	21.0	21.2	0.031	0.0098
L-PBF	19.0	17.8	20.0	21.5	21.6	0.045	0.0095

3. Results

3.1. As-printed microstructure and crystallographic texture

Similar compositions were measured for the L-DED and L-PBF samples, as listed in Table 1. A slightly lower content of Mn was detected in the L-PBF sample, which may arise from the high vapor pressure of Mn and higher frequency of melting during L-PBF processing with a much smaller laser beam size and thinner printing layer.

Neutron diffraction patterns of the L-DED and L-PBF CoCrFeMnNi HEAs are shown in Fig. 1c, which reveal the face-centered cubic (FCC) structure for both types of samples upon rapid solidification during laser additive manufacturing. The peak intensities of different crystallographic plane families are distinct, suggesting different textures in as-

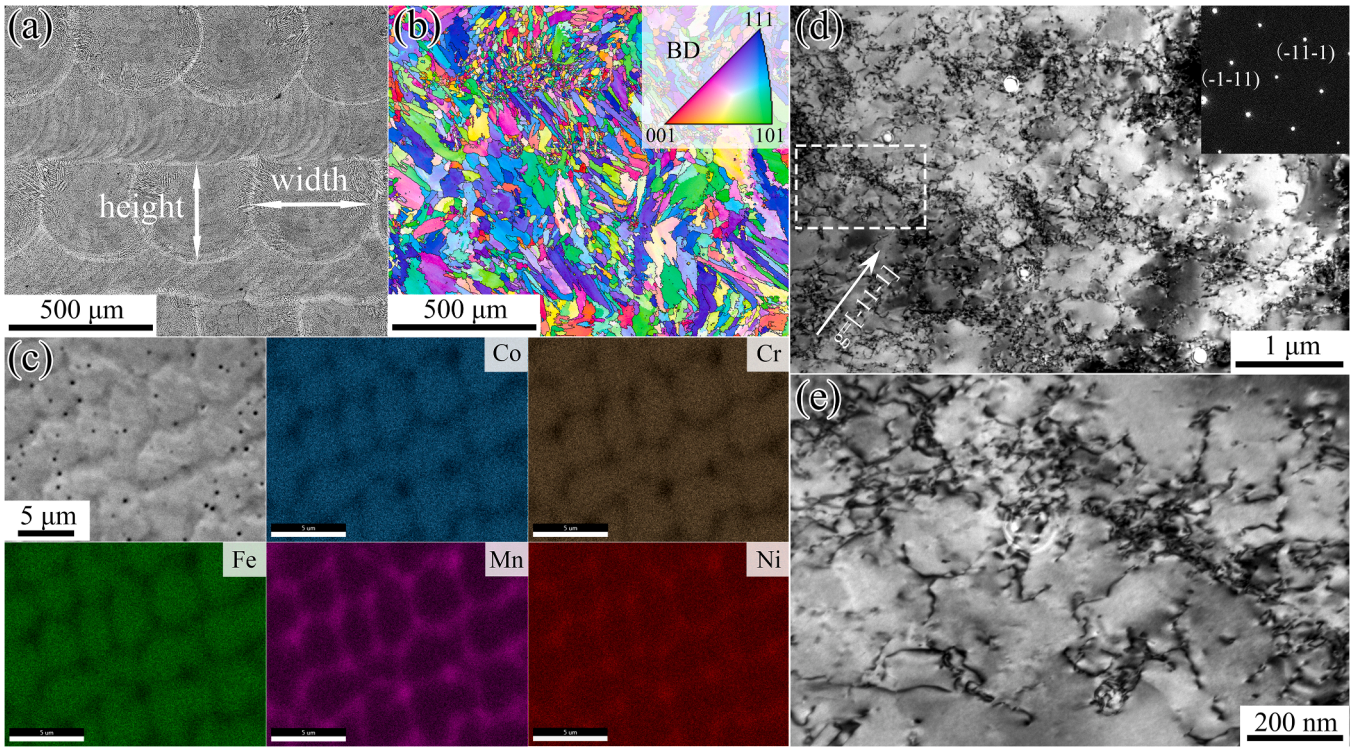

Fig. 2. Microstructure of the L-DED sample. (a) OM image of melt pools in the BD-LD plane; (b) IPF-BD of the BD-LD plane; (c) EDS maps of the BD-LD plane showing elemental segregation; (d) Low-magnification TEM image of the TD-LD plane showing dislocation entanglement and dense dislocation walls; (e) Magnified TEM image of the area marked by the dashed box in (d).

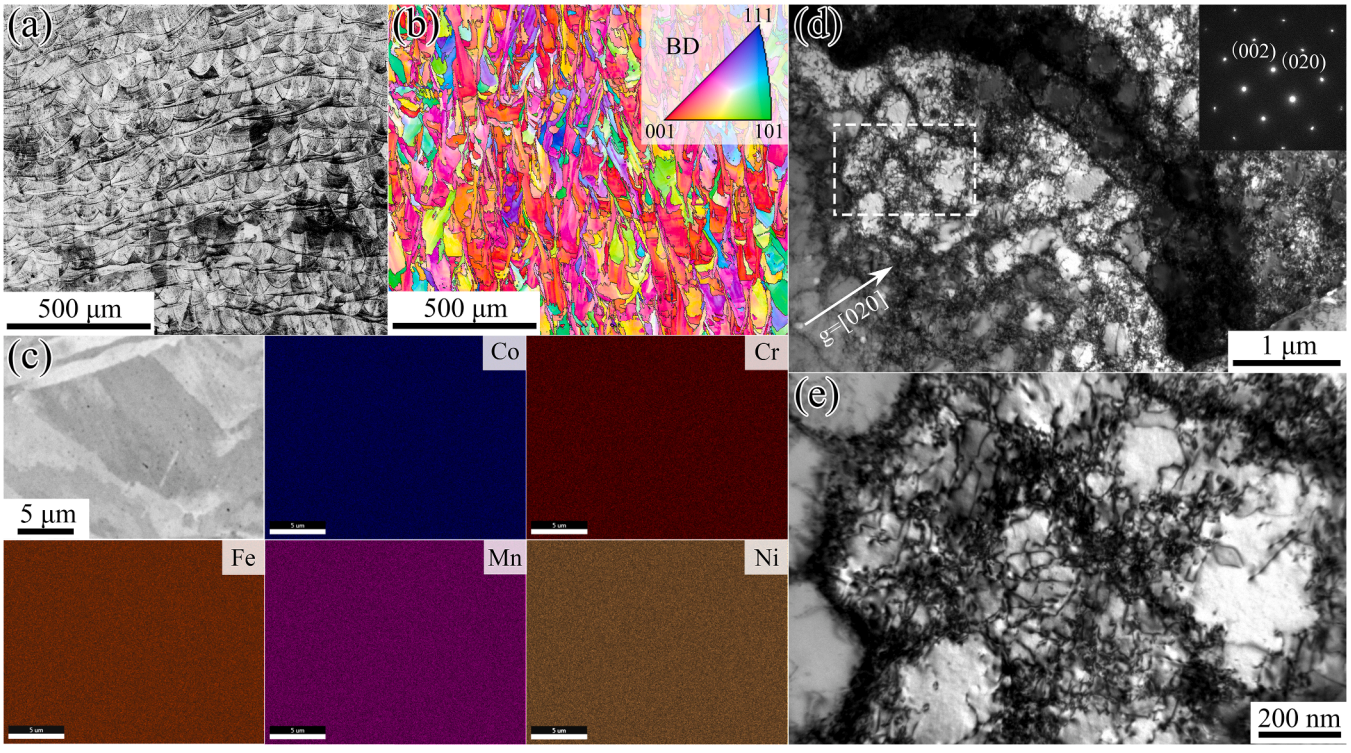

Fig. 3. Microstructure of the L-PBF sample. (a) OM image of melt pools in the BD-LD plane; (b) IPF-BD map of the BD-LD plane; (c) EDS maps of the BD-LD plane showing uniform elemental distribution without obvious elemental segregation; (d) Low-magnification TEM image of the TD-LD plane showing equiaxed dislocation cells; (e) Magnified TEM image of the area marked by the dashed box in (d).

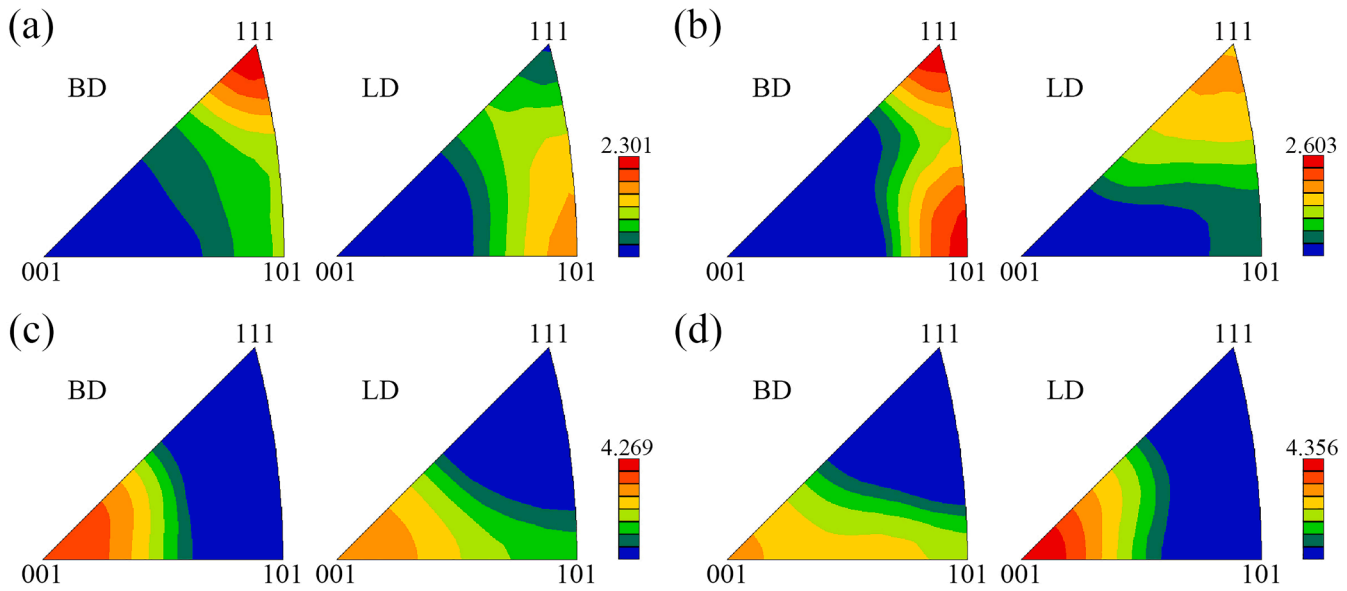

Fig. 4. Inverse pole figures of AM CoCrFeMnNi HEAs. (a) and (b) are exported from the BD-LD plane and TD-LD plane of the L-DED sample, respectively; (c) and (d) are exported from the BD-LD plane and TD-LD plane of the L-PBF sample, respectively.

printed samples, to be discussed later.

Fig. 2 shows the microstructure of a representative L-DED sample. A typical layer-wise morphology of the melt pools with "fish-scale" boundaries is visible, showing the overlap between adjacent melt pools/tracks (Fig. 2a). The melt pool is rather deep with a width of ~450 μm and height of ~370 μm, corresponding to a width-to-height ratio of 1.2. According to the inverse pole figure (IPF) map (Fig. 2b), elongated columnar grains grew along the BD with slight inclination to the LD due to perturbation of the heat flux associated with movement of the laser beam. The black lines delineate the tortuous grain boundaries with misorientation angles above 15°. Some equiaxed fine grains were observed at the top of melt pools within the interlayer regions. From the boundary to the center of the melt pool, the grain morphology gradually changes from columnar grains to equiaxed grains with an average grain size of ~49.6 μm. These changes can be attributed to spatial variations of the ratio of temperature gradient to growth rate (G/R) [24,25]. Of particular interest is the sub-grain solidification cell structures which are commonly observed in AM metals, and they form due to the effect of constitutional supercooling [26]. Compositional maps reveal chemical undulation across the cells due to segregation of Mn and Ni along the cell walls and enrichment of Co, Cr, and Fe in the cell interiors (Fig. 2c). Within these solidification cells, dislocation entanglement and some dislocation walls with an average spacing of ~1.7 μm were observed by TEM near the <110> zone axis with the diffraction vector g = [–11–1] excited (Fig. 2d). In addition, diffuse dislocation distributions were found in the cell interiors (Fig. 2e).

Fig. 3 shows the microstructure of a representative L-PBF sample. Repetitive melt pools were observed, with an average width of ~110 μm and height of ~60 μm, corresponding to a width-to-height ratio of 1.8 (Fig. 3a). Due to the much smaller laser beam size and hatch spacing in L-PBF, the melt pool size is substantially smaller but the width-to-height ratio is approximately 50% larger than that in the L-DED sample in Fig. 2. No obvious pores were detected, consistent with the nearly full density measured. Columnar grains were evident along the BD with an average grain size of ~53.6 μm (Fig. 3b), which is close to that of the L-DED sample. EDS analysis revealed relatively uniform elemental distributions with no apparent chemical segregation (Fig. 3c), in contrast to some previous work in which weak segregation of Mn and depletion of Fe were observed at the cell walls of the L-PBF CoCrFeMnNi sample [27]. Chemical homogeneity in our L-PBF sample is presumably due to

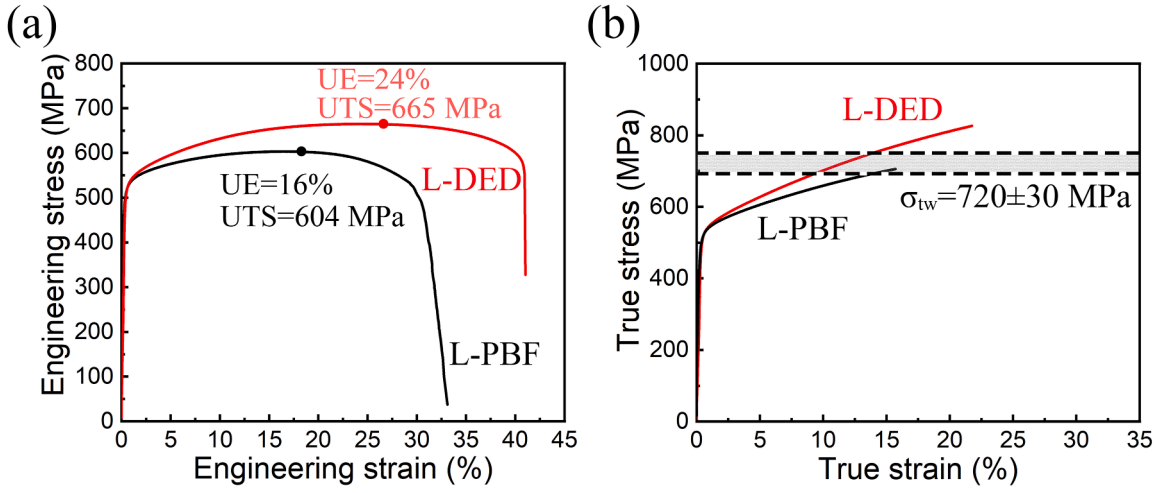

Fig. 5. Tensile properties of AM CoCrFeMnNi HEAs. (a) Engineering stress-strain curves; (b) True stress-strain curves.

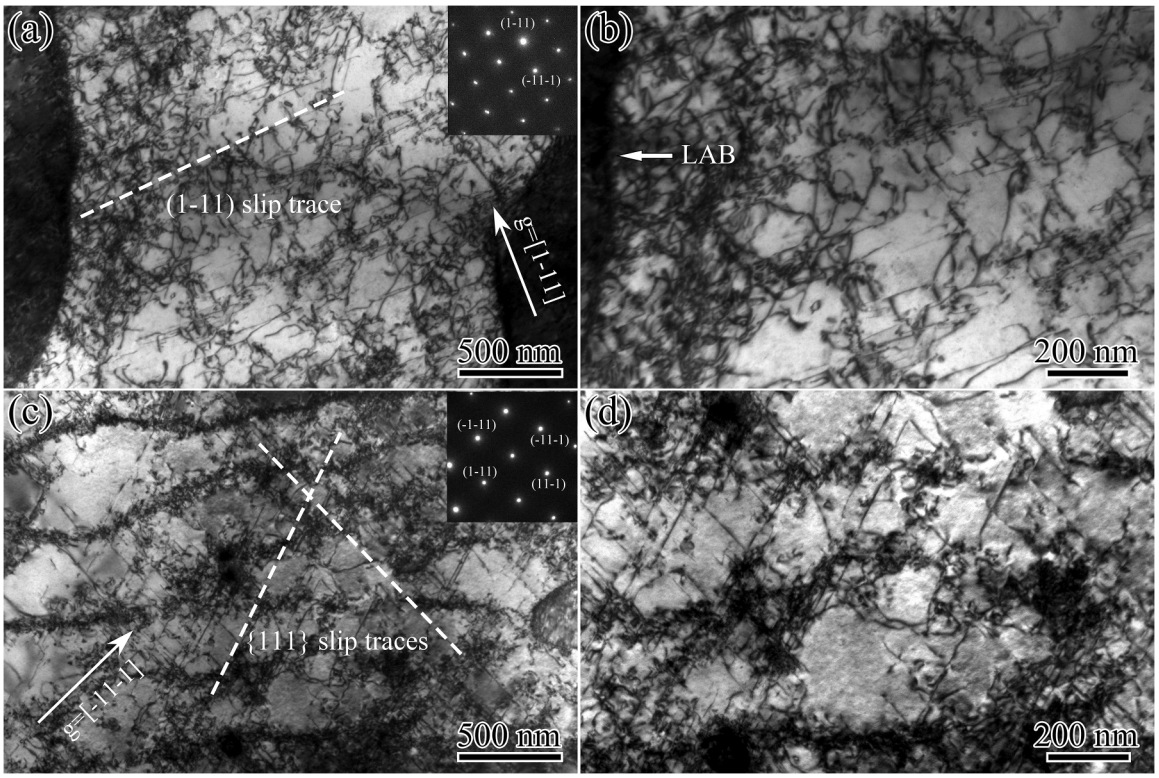

Fig. 6. Deformation microstructures of AM CoCrFeMnNi HEAs at 2% strain. (a) and (b) TEM images showing dislocation pile-up on the (1–11) slip plane at low-angle boundary (LAB) in the L-DED sample; (c) and (d) TEM images showing two sets of slip traces in the L-PBF sample.

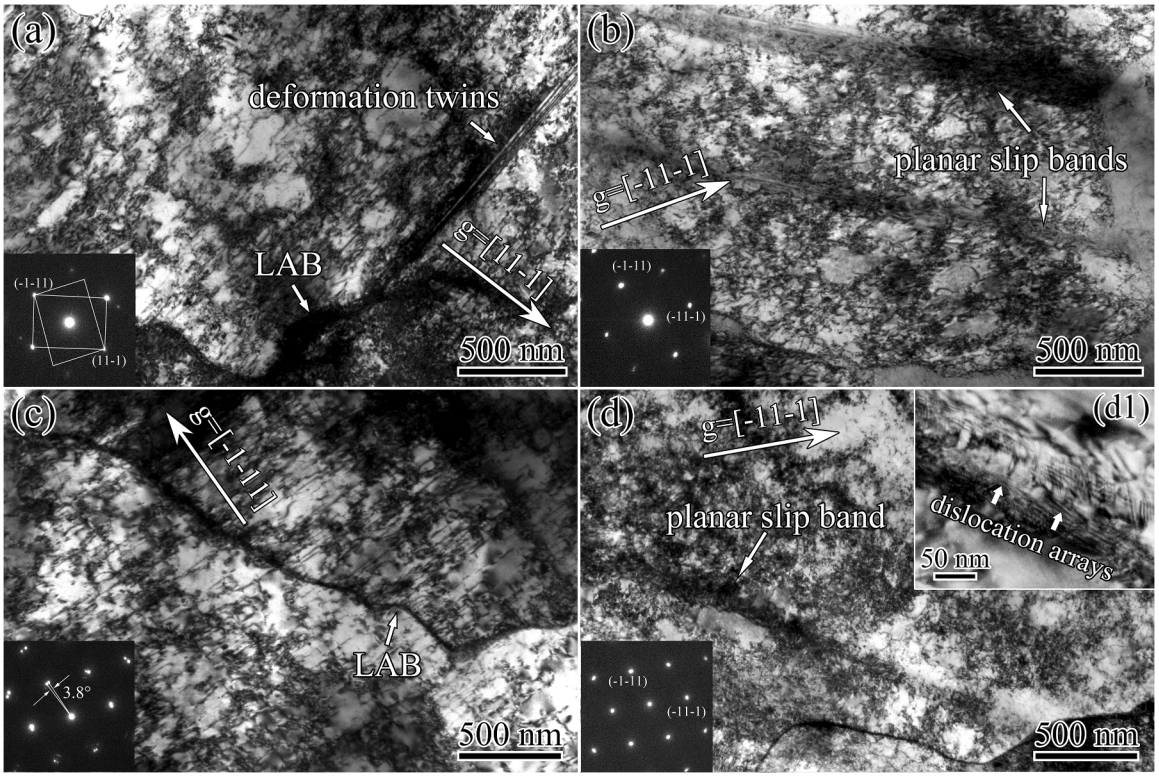

Fig. 7. Deformation microstructures of AM CoCrFeMnNi HEAs at 16% strain. (a) and (b) TEM images for the L-DED sample showing deformation twins and planar slip bands, respectively; (c) and (d) TEM images for the L-PBF sample showing dislocation obstruction by low angle boundary (LAB) and planar slip band, respectively; the inset (d1) shows pile-up of dislocation arrays at planar slip band.

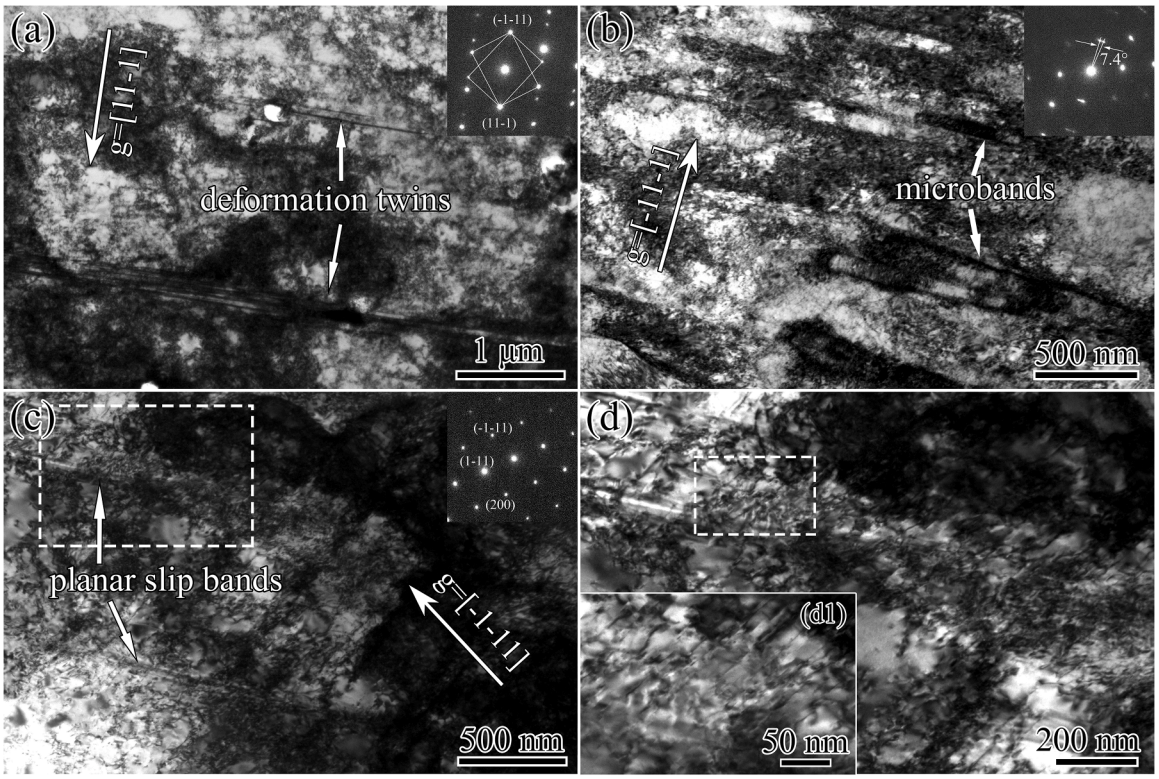

Fig. 8. Deformation microstructure of the L-DED sample at the necking strain (~24%). (a) TEM image of deformation twins; (b) Image of microbands; (c) Interaction between dislocations and planar slip bands; (d) Magnified image of the area marked by the dashed box in (c); the inset (d1) shows dislocation obstruction by planar slip bands.

the much higher cooling rate that suppressed elemental partitioning at the liquid/solid interface. Also different from the L-DED sample, more equiaxed and well-organized dislocation cells were developed in the L-PBF sample with a significantly smaller average cell size of ~0.4 μm (Fig. 3d). Most dislocations aggregated at the cell boundaries, leading to thicker dislocation walls than those in the L-DED sample. In the cell interiors, much lower densities of dislocations with diffuse distributions were observed (Fig. 3e). It has been reported that dislocation cell structures in L-PBF metal alloys arise due to cyclic thermal strains during repeated heating and cooling [8,28]. Such thermally-induced dislocation cell structures are analogous to those in materials under cyclic fatigue loading [29]. Overall, the higher cooling rate by L-PBF resulted in more refined solidification cells, well-developed dislocation cell structures, and less chemical segregation than L-DED.

A marked difference in crystallographic texture was observed between the L-DED and L-PBF samples (Figs. 2 and 3). The inverse pole figures of both BD-LD and TD-LD planes of the two types of AM samples were analyzed (Fig. 4). In the L-DED samples, a mixed texture of <101>/<111> was found along both BD and LD. In the L-PBF samples, both BD and LD present a strong <001> texture and a weak <101> texture. It has been well documented that the texture has a direct impact on the Taylor factor, which plays a critical role in the mechanical behavior of polycrystalline metals [30], to be discussed later.

3.2. Mechanical properties

Fig. 5 shows the tensile stress-strain curves of the AM CoCrFeMnNi HEAs. The L-DED and L-PBF samples exhibit the respective yield strengths of 515 ± 6 MPa and 505 ± 3 MPa, which are about two times those of conventional as-cast counterparts (Fig. 5a) [22]. The comparable yield strengths of the two types of AM samples are unexpected, considering a general trend of the increased yield strength with the decreased solidification cell size in AM metals [31]. The true stress-strain curves of these two types of AM samples are shown in Fig. 5b. The L-DED sample shows higher strain-hardening rates than the L-PBF sample, leading to simultaneously enhanced ultimate tensile strength (UTS) and uniform elongation (UE). Note that the shaded band in Fig. 5b represents the estimated range of critical stresses for deformation twinning (CST), which is approximately 720 ± 30 MPa for coarse-grained CoCrFeMnNi at room temperature [22]. Given the similar grain sizes in our study, other microstructural features (e.g., texture) could affect the CST. For the L-DED sample, the true flow stresses well surpass the CST range in the late stage of plastic deformation when the true strain exceeds 14%. In contrast, for the L-PBF sample, as the true stress just reaches the CST, necking instability sets in. This observation implies that the more sustained strain-hardening capability of the L-DED sample could be partly related to the enhanced deformation twinning activity.

3.3. Microstructural evolution

As shown in Figs. 2 and 3, the as-printed L-DED and L-PBF samples feature columnar grains with similar grain sizes. However, the sub-grain solidification cell structure, elemental distribution, and crystallographic texture in the two types of AM samples are markedly different and thus likely responsible for their different mechanical properties. To investigate their deformation mechanisms, the microstructural evolution at different tensile strains was studied by post-mortem TEM near the <110> zone axis with the diffraction vectors $g = <111>$ excited. At an initial strain of ~2%, dislocation slip dominated the plastic deformation in both L-DED and L-PBF samples (Fig. 6). Most dislocations appeared as long and straight lines, suggesting that planar slip was confined on the close-packed {111} planes.

At a large strain of 16%, we observed an increased amount of dislocations in the L-DED sample that facilitated the formation of dislocation tangles, well-organized dislocation cells, and planar slip bands

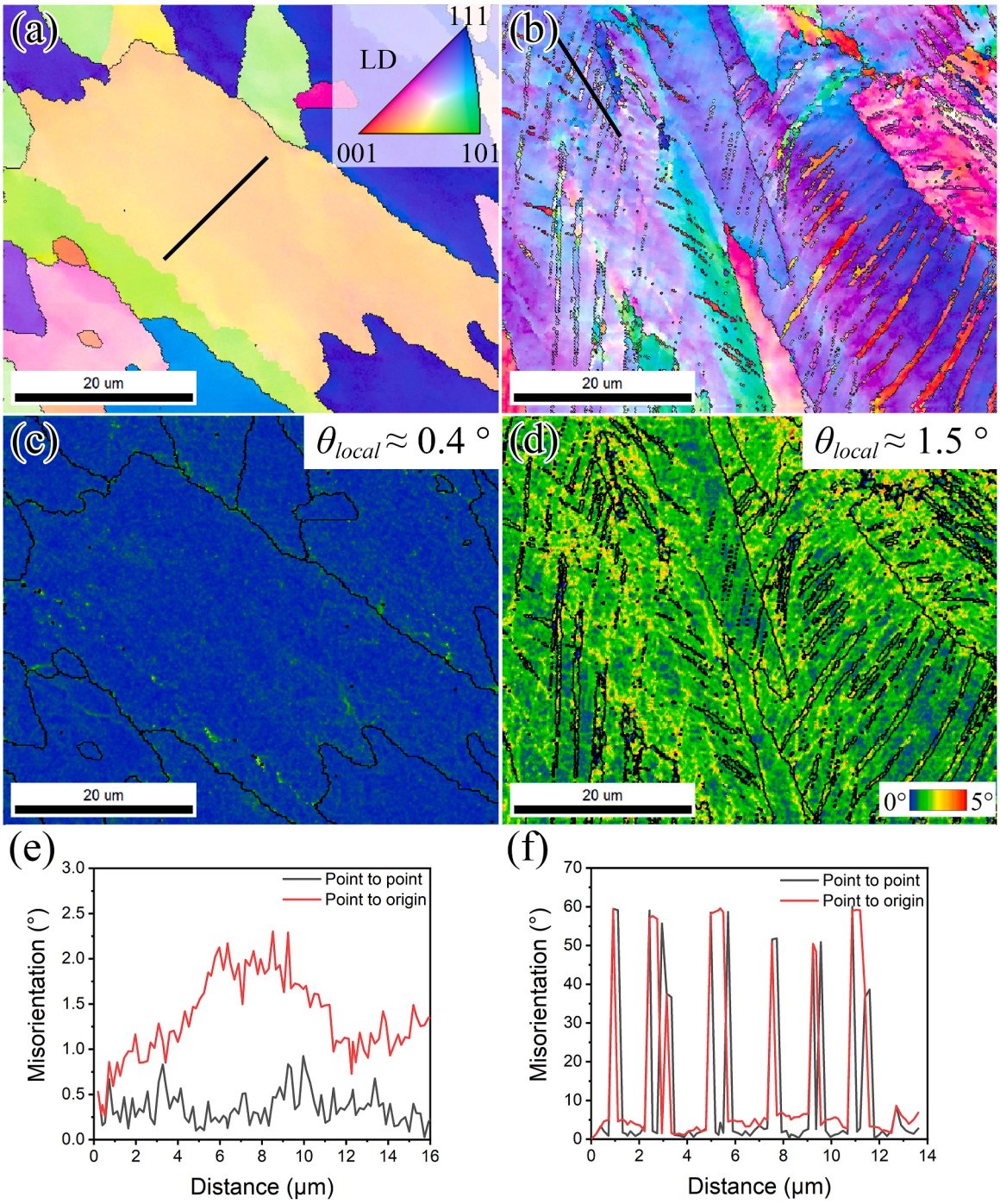

Fig. 9. Typical IPF images, KAM maps and distributions of misorientation of L-DED sample before and after tensile test. (a) and (b) IPF images obtained before and after tensile test, respectively; (c) and (d) KAM maps obtained before and after tensile test, respectively; (e) and (f) Plots of the misorientation angle variation measured with respect to the origin and from point to point along the black lines marked in (a) and (b), respectively.

(Fig. 7a and b). In addition, twinning was activated to produce plastic deformation, leading to sustained strain-hardening at high flow stresses. In contrast, necking instability was initiated at this strain in the L-PBF sample (Fig. 5), where the as-printed dislocation cells were largely retained (Fig. 7c). The high mechanical stability of the AM dislocation cell structures can be presumably attributed to the Lomer-Cottrell locks at the cell walls [19]. Abundant parallel dislocation slips were observed, and some of them propagated through the dislocation cell walls and were subsequently obstructed by low-angle boundaries (Fig. 7c). In some regions, the high density of dislocations resulted in highly tangled dislocation structures (Fig. 7d). Moreover, planar slip bands containing dislocation arrays were formed across dislocation walls through the movement of new slip lines [32]. It is noteworthy that unlike the L-DED sample, deformation twins were rarely observed in the L-PBF sample by post-mortem TEM.

Beyond the 16% strain, localized post-necking predominated tensile deformation of the L-PBF sample, leading to fracture at the necked region. In contrast, the L-DED specimen exhibited steady work hardening at high flow stresses. At the necking onset strain of ~24%, we analyzed the deformation microstructure in the L-DED sample. Both deformation twins and microbands were observed (Fig. 8a and b). Nanoscale deformation twins with thicknesses of 30–60 nm were frequently found

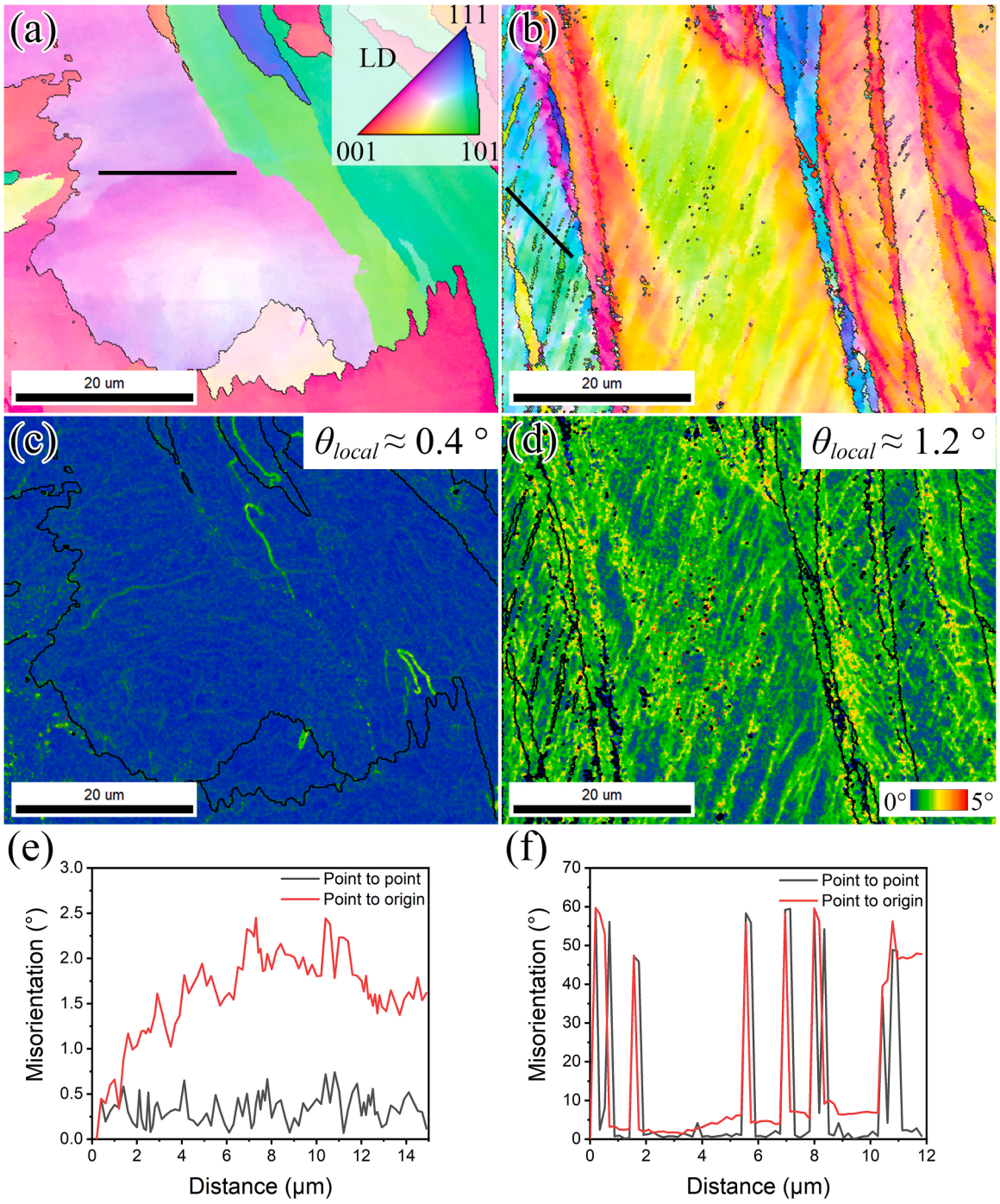

Fig. 10. Typical IPF images, KAM maps and distributions of misorientation of L-PBF sample before and after tensile test. (a) and (b) IPF images obtained before and after tensile test, respectively; (c) and (d) KAM maps obtained before and after tensile test, respectively; (e) and (f) Plots of the misorientation angle variation measured with respect to the origin and from point to point along the black lines marked in (a) and (b), respectively.

(Fig. 8a). Meanwhile, microbands with dense dislocation walls were aligned with the {111} slip planes (Fig. 8b). In the selected area diffraction (SAD) pattern, the diffraction spots were extended to arcs of 7.4°, indicating the formation of low-angle boundaries that were induced by dislocation multiplications and rearrangements during deformation. The morphology of these microbands is different from that observed in other FCC HEAs with low-to-medium stacking fault energies (SFEs) [33,34], but similar to that observed in high SFE materials after plastic deformation [35,36]. The formation of both deformation twin bands and microbands in crystalline metals seems uncommon since these two deformation mechanisms typically are favored in FCC metals with low and high SFEs, respectively [35]. The possible origin will be discussed in Section 4.3. Apart from the profuse deformation twin bands and microbands, parallel dislocations were hindered at the planar slip bands (Fig. 8c and d), which provided extra dynamic strain hardening.

We further analyzed dislocation multiplication and deformation twinning via EBSD characterization of the two AM CoCrFeMnNi HEAs before and after tensile tests. Typical IPF maps along with the corresponding kernel average misorientation (KAM) maps and misorientation maps are shown in Figs. 9 and 10 for the L-DED and L-PBF samples, respectively. The KAM maps were used to assess residual plastic strains [37]. In general, a higher KAM value suggests a larger residual plastic

Table 2
Statistical analysis of deformation twins in AM CoCrFeMnNi samples at the onset of necking.

Sample	Twin boundary fraction	Deformation twins per 2500 μm^2 scan area	Twin density (m^{-2})
L-DED	6.2%	111	4.4×10^{10}
L-PBF	1.2%	12	0.48×10^{10}

strain, accommodated by a locally increased density of geometrically necessary dislocations (GNDs). Before tensile test, the average KAM values in both L-DED and L-PBF samples were comparably low, with an average local misorientation of only ~0.4° (Figs. 9c and 10c). After deformation to necking, the average local misorientations in the L-DED and L-PBF samples reached ~1.5° (Fig. 9d) and ~1.2° (Fig. 10d), respectively. Significant increases in the average KAM values reflect strong dislocation multiplication in both samples after deformation. Apparently, the L-DED sample experienced stronger dislocation accumulation than the L-PBF sample. Moreover, the misorientation angles across the solidification cells for both AM samples were below 1° (Figs. 9e and 10f). Such intercellular misorientation variations are substantially lower than those across the dislocation walls in plastically deformed samples (>1.5°) [38]. The low-angle cell walls are helpful for maintaining the stability of the dislocation network and uniform strain-hardening [39]. In addition to dislocation multiplication, deformation twins were also identified in both types of AM CoCrFeMnNi samples (Figs. 9b and 10b), as confirmed by the orientation maps (Figs. 9f and 10f). A statistical analysis of deformation twins at the onset of necking based on the EBSD data is shown in Table 2. Drastically different twin densities of 4.4×10^{10} m^{-2} and 0.48×10^{10} m^{-2} were identified in the L-DED and L-PBF samples, respectively. The twin density in the L-DED sample well surpasses that in the L-PBF sample by one order of magnitude. We further studied the crystallographic orientation dependence of deformation twins in the L-DED sample by EBSD. Notably, deformation twins tended to occur in grains oriented close to the <111>//TA (tensile axis) (Supplementary Fig. S3). These grains generally possess larger Taylor factors ($M > 2.6$) and hence experience higher intensities of crystallographic shear under uniaxial tension. Furthermore, these grains with higher Taylor factors have multiple slip systems, which can promote dislocation accumulation and strain hardening that are necessary to induce twinning during deformation [40]. This also partially explains the observation that the L-PBF sample with <001> texture does not show profuse deformation twins, which is consistent with the general notion that deformation-induced twinning in FCC metals hardly occurs when $M < 2.6$ [40,41]. Altogether, our findings suggest that the more robust dislocation activities and deformation twinning collectively contribute to higher strain-hardening rates and flow stresses in the L-DED sample.

3.4. Thermally activated deformation behavior

To understand the microscopic mechanisms of plastic deformation

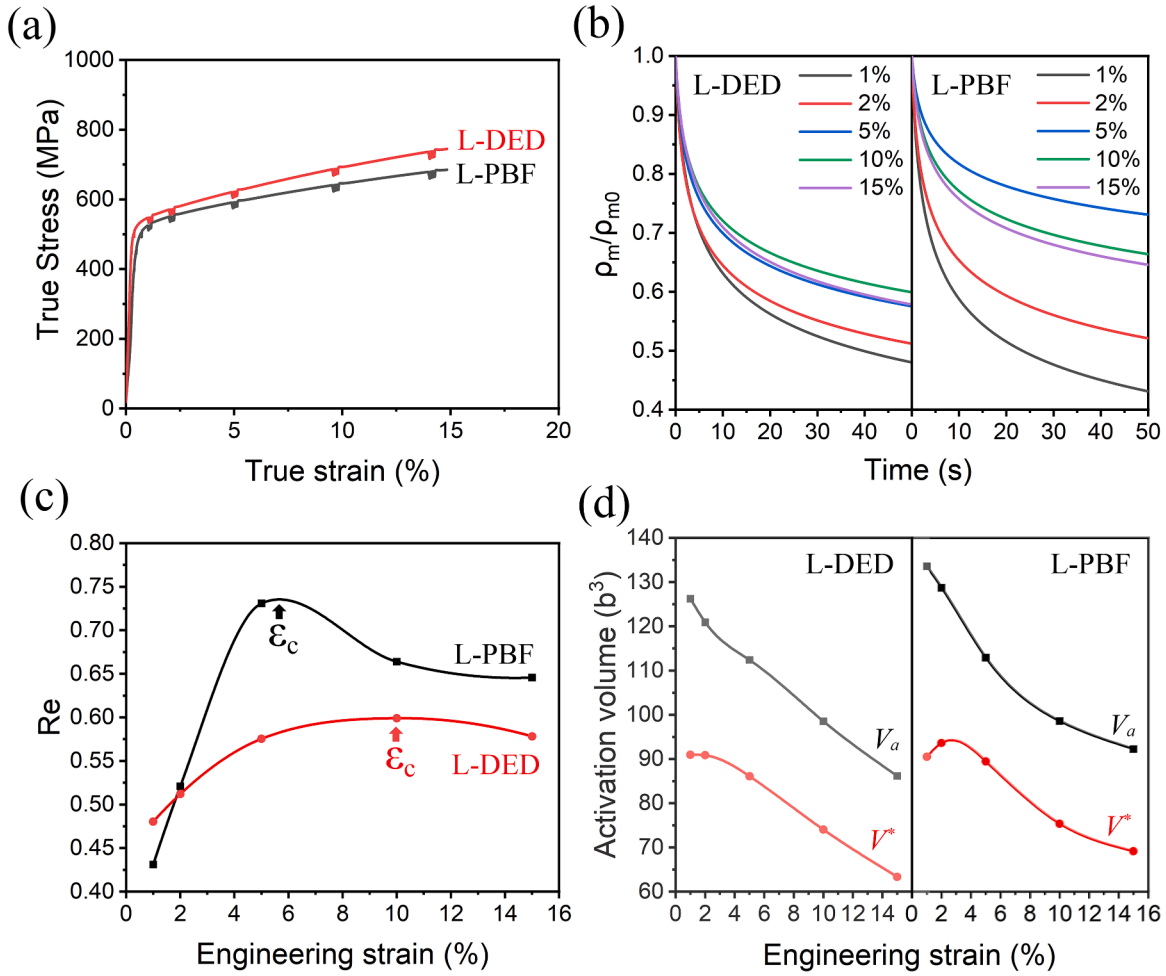

Fig. 11. Stress relaxation experiments of AM CoCrFeMnNi. (a) True stress-strain curves. (b) Evolution of mobile dislocation density versus time at various relaxation strains in L-DED (left) and L-PBF (right) samples; (c) *Re* versus engineering strain in L-DED and L-PBF samples; (d) Physical activation volume V^* and apparent activation volume V_a versus engineering strain in L-DED and L-PBF samples.

and hardening processes, stress relaxation experiments were conducted for both types of AM samples. Fig. 11a shows the true stress-strain curves from a series of stress relaxations at 5 interrupted strains. Thermal activation parameters of dislocations and their evolution were studied (Fig. 11b-d).

According to Caillard and Martin [42], the relative mobile dislocation density ($Re = \rho_m/\rho_{m0}$) is given by

$$\frac{\rho_m}{\rho_{m0}} = \left(\frac{C_r}{C_r + t}\right)^{\beta/(1+\beta)} \tag{1}$$

where ρ_m is the mobile dislocation density, ρ_{m0} the initial mobile dislocation density at the start of a relaxation transient, C_r a time constant, and β a dimensionless immobilization parameter. The β value can be calculated by

$$\beta = \frac{\Omega}{1 + K/E_M} - 1 \tag{2}$$

In Eq. (2), Ω is defined as $\Omega = V_a/V^*$, where V_a is the apparent activation volume and V^* the physical activation volume; K is the work-hardening coefficient calculated from the stress-strain curve, and E_M the elastic modulus of the specimen-machine assembly.

In each stress-relaxation transient, V_a and C_r can be determined by fitting the stress-relaxation curve according to

$$\Delta\tau = -\frac{k_B T}{V_a} \ln\left(1 + \frac{t}{C_r}\right) \tag{3}$$

where $\Delta\tau$ is the shear stress drop at time t, k_B the Boltzmann constant, and T the temperature. In repeated stress-relaxation transients, V^* can be determined by

$$V^* = k_B T \frac{\ln\left(\dot{\gamma}_{i2}/\dot{\gamma}_{f1}\right)}{\Delta\tau^*} \tag{4}$$

where $\dot{\gamma}_{i2}$ and $\dot{\gamma}_{f1}$ correspond to the shear strain rate at the start of relaxation 2 and the end of relaxation 1, respectively. The strain rate can be calculated by

$$\dot{\gamma} = (k_B T / E_M V_a)\left(\frac{1}{C_r + t}\right) \tag{5}$$

The applied shear stress consists of two components: the effective stress τ^* and the athermal stress τ_u. $\Delta\tau^*$ is the change of thermal component of the shear stress during relaxation. It is given by

$$\Delta\tau^* = (1 + K / E_M)\Delta\tau \tag{6}$$

Within the above framework, the thermal activation parameters of dislocations can be determined. In each stress relaxation, it is seen that the mobile dislocation density decreases with relaxation time in both L-DED and L-PBF samples (Fig. 11b). The stabilized relative mobile dislocation density after the first stress relaxation, *Re*, at different interrupted strains are also plotted (Fig. 11c). Specifically, *Re* in the L-DED sample increased with the increasing applied strain up to 10% and then slightly decreased upon further deformation to 15%. *Re* in the L-PBF sample also rapidly increased up to the strain of ~5%, then dropped continuously to approach a steady value after ~10% strain. In general, an increase of *Re* indicates dislocation accumulation while a decrease of *Re* often results from dislocation annihilation and/or dis-entanglement. Therefore, *Re* is a quantitative measure of the accumulation or exhaustion rate of mobile dislocations during deformation [43]. Here, we notice a transition from dislocation accumulation to dislocation exhaustion at a critical strain (ε_c) in both L-DED and L-PBF samples. The higher ε_c in the L-DED sample (~10%) than that in the L-PBF sample (~6%) suggests a more sustained dislocation storage capability in the former sample, which could be attributed to the larger solidification cell structures and the associated chemical undulation across the cells. The local lattice distortion arising from atomic size misfits in HEAs can lead to increased lattice resistance to dislocation glide [44]. The observed chemical undulation in the L-DED HEA occurs over a larger length scale than that in the random solid solutions of HEAs [5]. As such, the ruggedness of the energy landscape controlling the dislocation mobility becomes heightened, which can enhance the resistance to dislocation glide to promote extra strain hardening [45,46].

The flow stress of metallic materials is fundamentally affected by thermally activated processes such as dislocation slip and atomic diffusion [47]. Activation volume measurement provides insight into the rate-controlling deformation mechanisms. It should be noted that the physical activation volume V^* is different from the apparent activation volume V_a. According to Eqs. (1)-(6), V^* characterizes the sensitivity of dislocation velocity to stress and directly reflects the rate-controlling dislocation process, while V_a additionally incorporates the influence of mobile dislocation density [48]. As a result, V^* is more directly linked to the dislocation processes that are rate-controlling. Fig. 11d shows the measured V_a and V^* for the L-DED and L-PBF samples as a function of strain. In both types of AM samples, V_a is higher than V^* throughout the entire relaxation strain range. In the L-DED samples, both V_a and V^* exhibited rapid decreases with increasing strain. In the L-PBF sample, V_a decreased rapidly in the initial stage of relaxation and then gradually slowed down, and V^* firstly increased up to a strain of ~2% and then decreased continuously. The different trends of V^* in the two types of AM samples may originate from the difference in dislocation density and mobility in the initial stage of plastic deformation, which will be discussed later.

4. Discussion

4.1. Formation of as-printed microstructures

The large thermal gradient (G) and high cooling rate (R) inherent to L-DED and L-PBF processing result in non-equilibrium hierarchical microstructures, including columnar grains, solidification cells, dislocation structures, and elemental segregation. The solidification microstructure is highly dependent on constitutional supercooling at the liquid/solid interface, which is dictated by G and R. In general, the morphology of solidification structure is determined by the ratio of G/R, whereas the size of solidification structure is governed by the product of $G{\cdot}R$, namely, cooling rate during solidification [14,49]. Despite the similar average grain size (~50 μm) of the two AM CoCrFeMnNi alloys, the average size of sub-grain solidification cells in the L-DED sample is ~1.7 μm (Figs. 2c and d), which is significantly larger than that in the L-PBF sample (~0.4 μm), as shown in Figs. 3d and e. This is due to the lower cooling rates of 10^3–10^4 K/s during L-DED compared with 10^5–10^6 K/s during L-PBF [16].

Besides the different solidification cell sizes, the different cooling rates affect atomic diffusion and elemental distributions across the solidification cells in the L-PBF and L-DED samples. As shown in Fig. 3c, the higher cooling rate during L-PBF largely suppresses elemental segregation, leading to relatively uniform elemental distributions [13]. In contrast, chemical segregation coincides with the solidification cells to form chemical cells in the L-DED sample (Fig. 2c). Such chemical segregation originates from elemental partitioning (i.e., solute atom redistribution) at the solidification front. Our equilibrium thermodynamic calculation indicated that as the temperature drops during solidification, Ni and Mn are increasingly enriched in the remaining liquid while Fe, Cr, and Co are continuously partitioned to the solidified solid (Supplementary Fig. S4). This result agrees well with the experimental observation of enriched Fe, Cr and Co in the solidified cell interiors, as opposed to segregated Mn and Ni at solidified cell walls. The much lower cooling rate of L-DED compared to L-PBF could provide sufficient time for atomic diffusion during solidification and lead to significant elemental partitioning between cell interiors and cell walls, as also observed in other L-DED CoCrFeMnNi HEAs [18].

The different thermal schedules of L-PBF and L-DED processes also

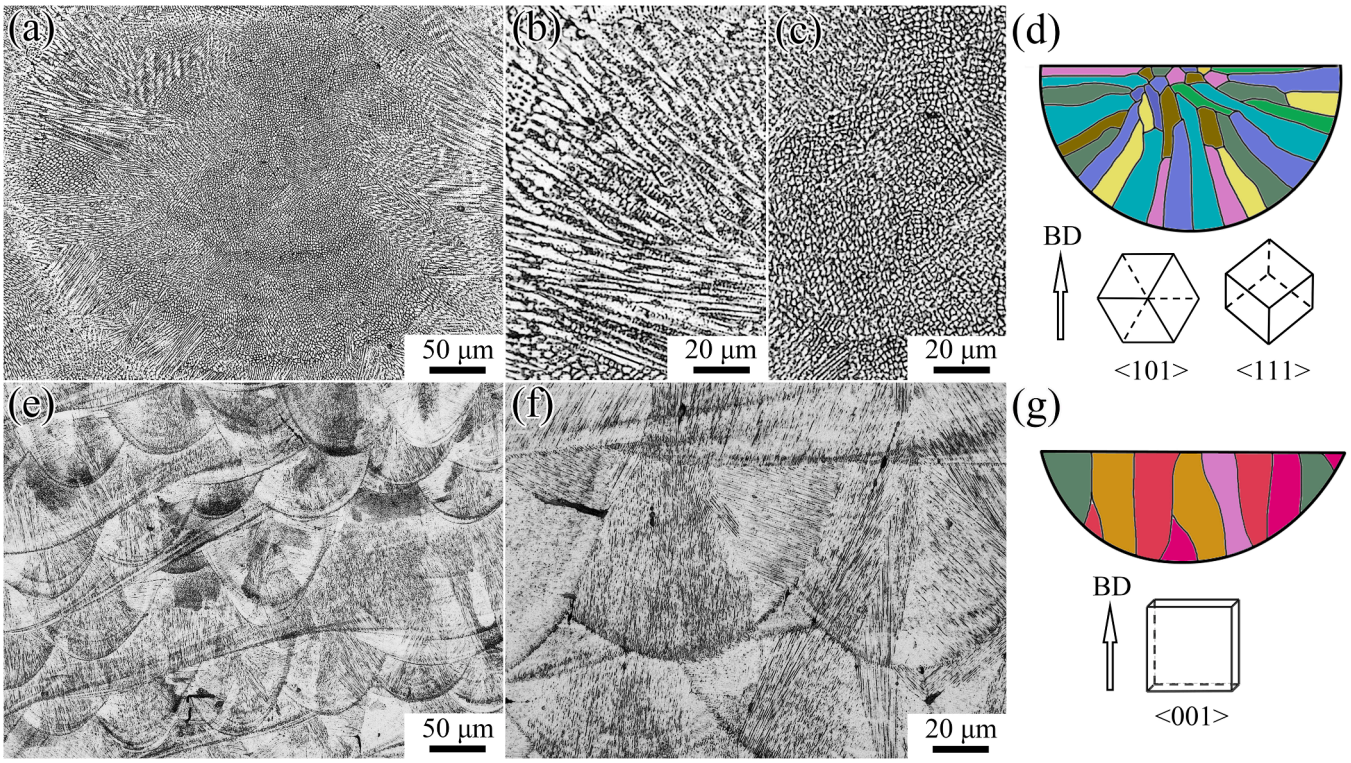

Fig. 12. Microstructure of AM CoCrFeMnNi HEAs. (a) Low-magnification OM image showing the morphology of melt pools in the L-DED sample and cellular dendritic grain growing from the local melt pool boundary toward the melt pool center; (b) and (c) Magnified OM images showing columnar dendrites at the melt pool boundary and cellular structures in the melt pool interior of the L-DED sample, respectively, indicating the heat extraction direction is in a radial manner; (d) Schematic diagram of preferred grain orientations (represented by different colors) with <101>/<111> along the BD in a melt pool of the L-DED sample; (e) Low-magnification OM image showing the morphology of melt pools in the L-PBF sample; (f) Magnified OM image showing the growth of finer cellular dendritic structures in the L-PBF sample across multiple layers of melt pools along the BD; (g) Schematic diagram of grain orientations (represented by different colors) with <001> along the BD in a melt pool of the L-PBF sample.

result in distinct dislocation structures in the solidification cells. During laser additive manufacturing, thermomechanical stresses/strains caused by localized heating/cooling cycles are responsible for the generation of dislocations [50]. Such stresses can be sufficiently large and even exceed the yield strength of the material at elevated temperatures during solidification, thereby triggering the formation of dislocations. The specific thermal schedule during additive manufacturing plays an important role in the development of residual stresses and the temporal/spatial evolution of these printing-induced dislocations. Due to the much smaller laser beam size and print layer thickness, the L-PBF sample underwent more repetitive thermal cycles, and the dislocations were self-organized into dislocation cells with a high density of dislocations aggregated at the cell boundaries (Figs. 3d and e). In contrast, the different thermal history in the L-DED sample resulted in more diffuse dislocations and less well-developed dislocation cells (Figs. 2d and e). Previous work revealed that chemical micro-segregation is not a prerequisite for the formation of dislocation cells, but the compositional heterogeneity (e.g., chemical cells) associated with the solidification cells may provide a strong pinning resistance to dislocation motion [50–52].

The different textures in the two AM HEAs arise likely due to the differences in the shape and size of the melt pools dictated by the laser beam size and energy density input in L-DED and L-PBF processes. Epitaxial and competitive growth mechanisms are dominant during additive manufacturing. In general, grain growth is favored when the direction of the steepest temperature gradient (perpendicular to the local melt pool boundary) aligns with the easy-growth direction (<001> for cubic crystals) [53]. When the above two directions are well aligned, epitaxial growth from pre-existing grains dominates, which promotes the formation of elongated columnar grains that extend through multiple layers to form a strong <001> fiber texture along the BD [54]. However, due to local perturbations of heat flux, solidified grains may also shift their growth directions toward new directions along local temperature gradients [55]. These new growth orientations may be no longer preferable for continuous growth, leading to competitive growth (or side-branching) of cellular dendrites even inside a melt pool [53]. Previous study on the relationship between melt pool geometry and crystallographic texture by kinetic Monte Carlo simulations unveiled the texture transition from <101> to <001> with the increase of width-to-height ratio of the melt pool [56]. In our work, the L-DED sample features relatively narrow and deep melt pools with an average width-to-height ratio of 1.2 and forms a mixed texture of <111>/<101> along the BD (Figs. 2 and 4). In contrast, the L-PBF sample exhibits a relatively large width-to-height ratio of 1.8 and forms a strong <001> texture with a weak <101> texture along the BD (Figs. 3 and 4). A melt pool with a small width-to-height ratio promotes the buildup of thermal gradients in a radial manner, resulting in solidification with the <001> grains growing from the local melt pool boundary toward the melt pool center. As such, epitaxial growth with <101> orientation along the BD is formed (Fig. 12a-d). In comparison, a melt pool with a large width-to-height ratio enlarges the remelting regions, thus facilitating the alignment of maximum thermal gradient direction along the BD and consequently epitaxial growth across multiple layers with <001> orientation along the BD (Fig. 12e-g). In addition, competitive growth occurs under the influence of local heat flux perturbations in the dynamic melt pools, leading to the weak <101> texture in the L-PBF sample and the <111> texture in the L-DED sample along the BD. Hence, the development of different textures in the two types of AM samples results from the competition between the alignment of easy-growth directions and the directions of local thermal

Table 3
Theoretical estimates of yield strength in L-DED and L-PBF samples, as compared with experimental measurements.

Sample	D (μm)	M	ρ (m^{-2})	τ_0 (MPa)	τ_d (MPa)	τ_ρ (MPa)	$\sigma_{y,theo}$ (MPa)	$\sigma_{y,exp}$ (MPa)
L-DED	19.8	3.32	3.71×10^{14}	41	36	78	515	515
L-PBF	9.7	2.89	3.47×10^{14}	41	52	76	488	505

gradients [54].

4.2. Strengthening mechanisms

Despite the much lower cooling rate and larger solidification cells in the L-DED samples than the L-PBF samples, their yield strengths are comparable. To understand this result, we consider several operative strengthening mechanisms in both types of AM samples. The strengthening of a polycrystalline material generally arises from solute atoms, grain boundaries, dislocations, and precipitates, among others. Solid solution strengthening occurs when the alloying atoms are present and differ from the matrix atoms in size and bond stiffness, which can result in an atomically varying lattice strain field [57]. For the equiatomic CoCrFeMnNi alloy, the atomic radii between different constituent elements are similar, such that atomic-level variations of the lattice strain field could be limited. Nonetheless, the solid solution strengthening effect should exist with the presence of five types of concentrated alloying elements, and thus increase both the lattice friction stress and Hall-Petch coefficient [18]. Few precipitates were observed in AM CoCrFeMnNi and hence the contribution of precipitation strengthening is negligible. Other strengthening mechanisms that we considered for the two types of AM CoCrFeMnNi HEAs include the strengthening effects from grain boundaries and dislocation interactions (e.g., cutting of forest dislocations). In a first-order approximation of the effect of texture, the yield strength σ_y is estimated by

$$\sigma_y = M(\tau_d + \tau_\rho) \tag{7}$$

where M is the Taylor factor; τ_d and τ_ρ are the effective resolved shear stresses within grains contributed by grain boundaries and dislocation interactions, respectively. M depends on the crystallographic texture with respect to the tensile axis, as well as on the Schmid factor and the number of active slip systems [30]. The mean Taylor factors exported from our EBSD data for the L-DED and L-PBF samples are 3.32 and 2.89, respectively. Such difference in the Taylor factor arises largely from the different textures in the two types of AM samples (Fig. 4).

To account for the grain boundary strengthening effect, τ_d can be estimated by [58]

$$\tau_d = \tau_0 + k_s D^{-1/2} \tag{8}$$

where τ_0 is the lattice friction stress, k_s the shear stress intensity for transmission of plastic flow at grain boundaries, and D the average grain size or boundary spacing. The values of $\tau_0 \approx 41$ MPa and $k_s \approx 161$ MPa·$\mu m^{1/2}$ are derived from a linear fit of the Hall-Petch relationship for the CoCrFeMnNi alloy with a random texture ($M = 3.06$) [59]. It has been recognized that AM alloys often contain a large fraction of sub-grain dislocation boundaries with misorientation angles above ~2° (i.e., low-angle grain boundaries), which play a key role in strengthening [7, 60]. Hence, the boundaries with misorientation angles higher than 2° are considered to estimate the grain boundary strengthening. Based on the EBSD results with the step size of 0.2 μm, the average D values of the L-DED and L-PBF samples are determined to be 19.8 μm and 9.7 μm, respectively, giving the respective τ_d of 36 MPa and 52 MPa, as summarized in Table 3.

The strengthening effect from dislocation interactions can be estimated by [61]

$$\tau_\rho = \alpha G b \sqrt{\rho} \tag{9}$$

where α is an effective constant, G shear modulus, b the Burgers vector length, and ρ the initial dislocations density. For the CoCrFeMnNi HEA, α, G, and b are estimated to be 0.2, 80 GPa, and 0.254 nm, respectively [18]. To estimate ρ, we note that during additive manufacturing, printing-induced dislocation networks arise from cyclic thermal stresses induced by repeated laser scanning [50]. According to the modified Williamson-Hall method [62] (see Appendix A), we measured ρ based on the line profile analysis of neutron diffraction patterns of as-printed samples (Fig. 1c). The estimated ρ value in the L-DED and L-PBF samples is 3.71×10^{14} m^{-2} and 3.47×10^{14} m^{-2}, giving τ_ρ of 78 MPa and 76 MPa (Table 3), respectively.

The yield strengths from the above theoretical analyses and experimental measurements are listed in Table 3. The predicted yield strengths ($\sigma_{y,theo}$) agree well with the measured values ($\sigma_{y,exp}$) for both the L-DED and L-PBF samples. Given the lower grain boundary strengthening and higher Taylor factor of the L-DED sample, the comparable yield strengths for the two AM samples are attributed to the complementary effects of boundary spacing and crystallographic texture. Our results are at variance with the notion that the yield strength of AM FCC metal alloys can be correlated to the solidification cell size [9,18-20], and thus underscore the critical impact of solidification texture on the mechanical properties of AM metal alloys.

4.3. Deformation mechanisms

4.3.1. Dependence of activation volume on deformation mechanism

The physical activation volume is proportional to the number of atoms involved in the thermally-activated rate-controlling process, such that it measures the individualistic and collective nature of transition [42]. It has been reported that the characteristic range of the physical activation volume $V^* \approx 0.1$–$1\ b^3$, $V^* \approx 1$–$50\ b^3$, and $V^* > 50\ b^3$ correspond to the dominant rate-controlling mechanism of lattice diffusion, grain boundary mediated plastic deformation, and forest dislocation cutting, respectively [47]. Hence, the activation volume can serve as an effective signature of the rate-controlling mechanisms in metals and alloys [63]. For both the L-DED and L-PBF CoCrFeMnNi samples in our work, the measured V^* values fall in the range of 60 b^3 to 90 b^3. Such measured activation volumes could be dictated by the combined effects of the elevated lattice friction from concentrated solute atoms and the increased slip resistance from the forest dislocations with high densities that originate from thermal cycling during additive manufacturing and further rise with plastic straining [42]. For the L-DED samples, V^* continuously decreased with increasing strain, suggesting the increased dislocation density with plastic straining. The solidification cell walls in the L-DED samples can serve as strong barriers against dislocation transmission due to chemical segregation at the solidification cell walls. This effect can presumably reduce V^* in the L-DED samples. In comparison, V^* in the L-PBF samples first increased with increasing strain up to ~2%. This unusual increase of V^* could be attributed to the deformation-induced relaxation of printing-induced dislocations, leading to an initial decrease of dislocation density. The subsequent decrease of V^* could stem from the deformation-induced increase of dislocation density. Overall, the measured differences in the strain-dependent activation volumes between the two types of AM samples reveal the impact of printing-induced dislocation structures and their evolution during subsequent plastic deformation.

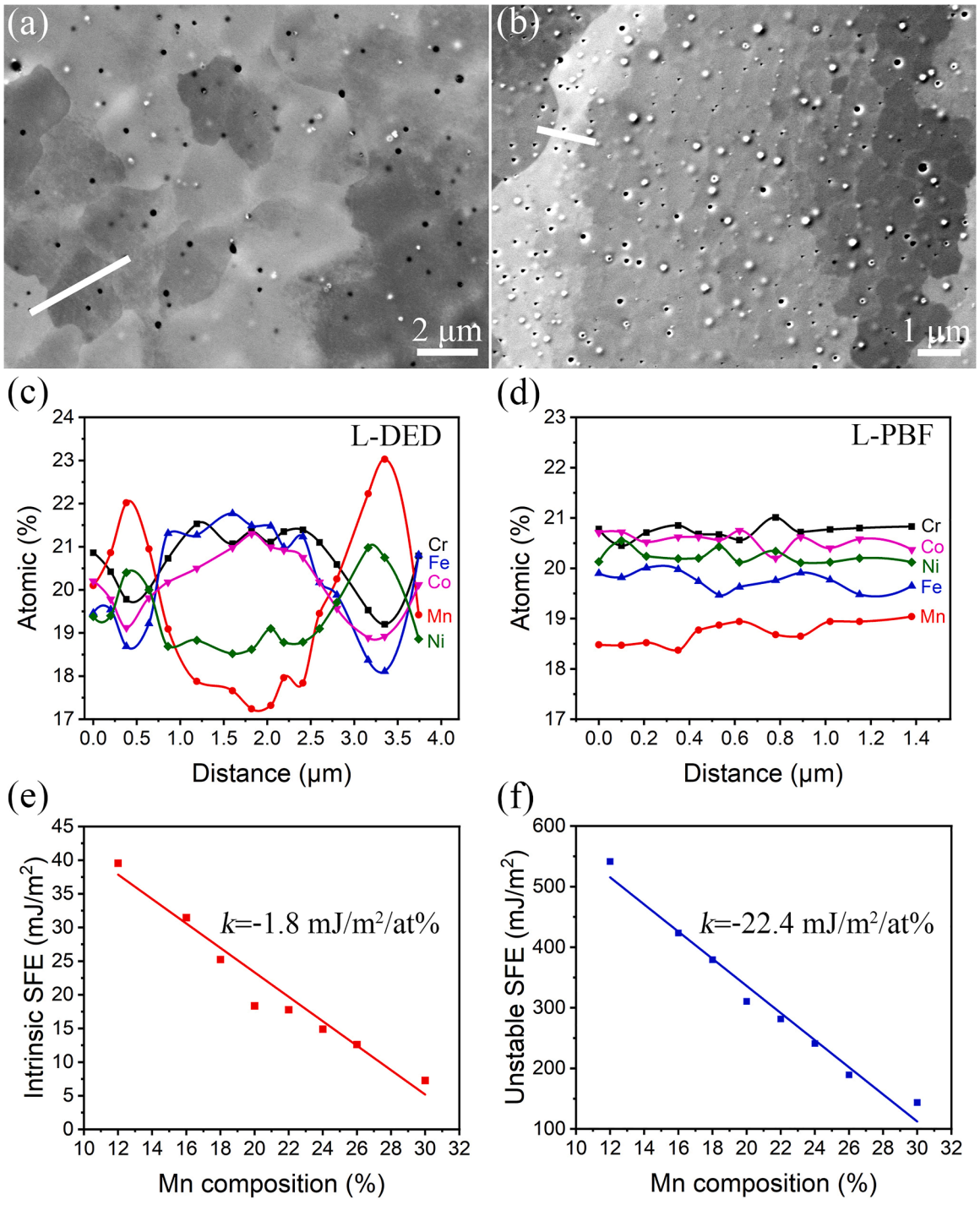

Fig. 13. Elemental distributions and SFE fluctuations in AM CoCrFeMnNi. (a) and (b) SEM images of L-DED and L-PBF samples, respectively (small holes from pitting corrosion during sample preparation); (c) and (d) Elemental distributions along the white lines across the solidification cell boundaries in (a) and (b), respectively; (e) and (f) Intrinsic SFE and unstable SFE against Mn composition in CoCrFeMnNi from first-principles calculations, respectively.

4.3.2. Formation of planar slip bands and microbands

Planar slip bands were observed in both L-DED and L-PBF samples at the strain of ~16% (Fig. 7). These planar slip bands, also known as "persistent Lüder bands" (PLBs), are generated by pronounced planar slip and rearrangement of dislocations [64]. Two physical mechanisms have been proposed to explain the formation of PLBs in FCC metals [65]: (1) The low SFE inhibits cross-slip due to the wide stacking fault between the leading and trailing partials of dissociated dislocations. (2) The presence of short-range ordering (SRO) leads to a glide plane softening phenomenon, represented by an array of succeeding dislocations following a leading dislocation on the same glide plane. Although SRO has been reported in HEAs [5], there is still a lack of strong evidence of SRO in the widely studied CoCrFeMnNi HEA.

To understand the mechanistic origin of PLBs in AM CoCrFeMnNi, we performed first-principles calculations (see Appendix B) to quantify the intrinsic and unstable SFEs based on the experimentally measured compositions across the solidification cells for both L-DED and L-PBF samples, as shown in Fig. 13. Considering that the Mn content is more sensitive to the entropy of mixing in the CoCrFeMnNi system [66] and has the largest amplitudes of fluctuation across the solidification cells in

the L-DED samples (Fig. 13a, c) compared to the L-PBF samples (Fig. 13b, d), the intrinsic and unstable SFEs as a function of Mn content were investigated. The unstable SFE can be correlated to the energy barrier of formation of partial dislocations, and it is the maximum value along the generalized SFE curve with shear displacement along the partial slip direction [67,68]. It is seen from Fig. 13e and f that both intrinsic and unstable SFEs decrease with Mn content. With the increased Mn content, the variation of the unstable SFE (−22 mJ/m^2/at %) is much larger than that of the intrinsic SFE (−1.8 mJ/m^2/at%). These results indicate that the intrinsic SFE fluctuates in the range of 17–29 mJ/m^2 for the L-DED samples while it maintains a relatively constant value of ~25 mJ/m^2 for the L-PBF samples. Such low SFEs and high frictional stresses are likely responsible for the formation of PLBs in both L-DED and L-PBF samples [69]. For the L-DED samples, since unstable SFE is more sensitive to the Mn content, the barrier for partial dislocation nucleation decreases significantly in the high Mn region. For example, the unstable SFE for the high Mn region (23 at%) in L-DED CoCrFeMnNi is approximately as low as 260 mJ/m^2, which could promote planar slip of dislocations. Therefore, the chemical heterogeneity in the L-DED samples could further elevate the Peierls stress and local variations of unstable SFEs, promoting the formation of PLBs. It is noteworthy that PLBs can serve as strong obstacles for dislocation motion on other slip systems and thus enhance strain hardening during plastic flow.

It is surprising that additional microbands were frequently observed at 24% strain in the L-DED CoCrFeMnNi (Fig. 8b). This stands in contrast with the general observation that microbanding typically operates in materials with high SFEs above 90 mJ/m^2 [70]. Despite the low SFEs, the microbands in the L-DED sample share a similar morphology to those in the high SFE materials such as Ni and Al [35]. Two possible mechanisms have been proposed for microbanding-mediated plastic deformation in FCC materials, i.e., the double cross-slip mechanism and the dislocation boundary splitting mechanism [71]. In both mechanisms, dislocation cross-slip is a key to initiation of microbanding. Specifically, in the first mechanism, microbanding arises due to pronounced dislocation cross-slip activity, which allows microbands to accommodate modest lattice rotations with misorientation angles below 1°. In the second mechanism, microbands arise from the development of dislocation rearrangement and dislocation wall splitting at higher local stresses, leading to grain subdivision and new domain boundaries with misorientation angles above 1° to accommodate large lattice rotations. Dislocation cross-slip as a precursor to microbanding has been revealed by both stress relaxation (Fig. 11d) and TEM studies (Figs. 7 and 8). Our TEM analysis of the microband shows a misorientation angle of 7.4° (Fig. 8b), indicating that microbanding in the L-DED CoCrFeMnNi could result from the dislocation boundary splitting mechanism. Note that microbands were not observed in the L-PBF sample, possibly because of the insufficient dislocation accumulation and comparatively lower local stresses that are incapable to trigger adequate dislocation cross-slip for splitting of the dislocation walls. In fact, microbands have been previously observed in CoCrFeMnNi under a high strain rate (8×10^3/s) due to increased flow stresses, but not under quasi-static strain rates [34]. The microbanding behavior of the L-DED sample during quasi-static deformation is uncommon. The high flow stresses in this type of AM samples can be understandably attributed to the strong dislocation accumulation capability (evidenced by the large local misorientations, Fig. 9d) and chemical undulation associated with the solidification cells. Both the pronounced dislocation accumulation and the chemical heterogeneity can enhance the resistance to dislocation glide, leading to elevated local stresses and stronger dislocation interactions to facilitate dislocation cross-slip and thus microbanding. The resulting multiple microbands, on one hand, can offer additional strain hardening by dynamic grain subdivision in a way analogous to low-angle grain boundaries. On the other hand, microbands provide alternative modes for strain delocalization through dislocation cross-slip and therefore promote more sustained plastic deformation [72].

4.3.3. Deformation twinning

Deformation twinning in FCC materials is closely related to the formation and reactions of stacking faults [73]. Deformation twins are formed by glide of Shockley partial dislocations of the same type on successive {111} planes. In general, stacking faults are generated by dissociation of perfect dislocations of the type $a/2<110>$ into leading and trailing Shockley partial dislocations of the type $a/6<211>$ (a is the lattice constant) [35]. The critical resolved shear stress to separate the leading Shockley partial from its trailing counterpart can be estimated by [74]

$$\tau_{cr} = \gamma_{sf}/b_p \tag{10}$$

where γ_{sf} is the SFE and b_p is the Burgers vector length of a Shockley partial dislocation. Considering that the glide dislocations experience a frictional drag, the separation distance of partial dislocations will depend on their velocities as well as direction and magnitude of the uniaxial stress. According to Copley and Kear [75], the Shockley partial separation distance d_p can be estimated by

$$d_p = \frac{Gb_p^2}{8\pi\gamma_{eff}} \tag{11}$$

$$\gamma_{eff} = \gamma_{sf} \pm \frac{m_T - m_L}{2}\sigma b_p \tag{12}$$

where γ_{eff} is the effective SFE; m_T and m_L are the Schmid factors of the trailing and leading partials, respectively; σ is the uniaxial stress and the $\pm$ sign denotes tension (+) and compression (−). Since m_T is generally different from m_L, the Shockley partial separation distance d_p becomes orientation-dependent.

To attain a large separation distance between leading and trailing partials for nucleation and growth of deformation twins, a low effective SFE is necessary. In this work, deformation twins were observed in both types of L-DED and L-PBF samples, but mostly in grains with the orientations close to <111>//TA Figs. 9,10 and Supplementary Fig. S3). The <111>-oriented grains have the Schmid factors of $m_T = 0.16$ and $m_L = 0.31$ during tensile deformation, giving an orientation factor $(m_T - m_L)/2 = -0.075$ [76]. Substituting such negative orientation factor into Eqs. (11) and (12) gives a reduction in effective SFE and correspondingly an increase in d_p, promoting the formation of intrinsic stacking faults and twinning. In comparison, the <001>-oriented grains have the Schmid factors of $m_T = 0.47$ and $m_L = 0.23$, giving $(m_T - m_L)/2 = 0.12$ such that the increased effective SFE and decreased d_p promote cross slip [77]. Hence, the higher twin density of 4.4 $\times 10^{10}$ m^{-2} found in the L-DED sample (Table 2) is attributed to the high volume fraction of grains with the <111>//TA orientation. In contrast, the L-PBF sample contains a preferred texture of <001>//TA, resulting in the comparatively smaller twin density of only 0.48 $\times 10^{10}$ m^{-2}. It should be noted that under some extreme experimental conditions such as cryogenic temperatures, the sufficiently high external stresses can cause the "re-dissociation" phenomenon of a perfect dislocation in the <001>-oriented grains, i.e., exchange of the normal sequence of Shockley partial dislocations, which could result in the formation of extrinsic stacking faults and twinning nucleation [78,79].

In addition to the small effective SFE and the large Shockley partial separation distance discussed above, a high flow stress is also necessary to promote nucleation and growth of deformation twins. The higher Taylor factor, greater dislocation storage capability, as well as the interplay between dislocations and chemical undulation in the solidification cell structures of the L-DED samples can elevate the flow stress to well surpass the critical stress for twinning. The enhanced deformation twinning together with the active operation of both planar dislocation slip and microbanding enable higher work hardening rates and thus larger ductility of the L-DED samples compared to the L-PBF samples.

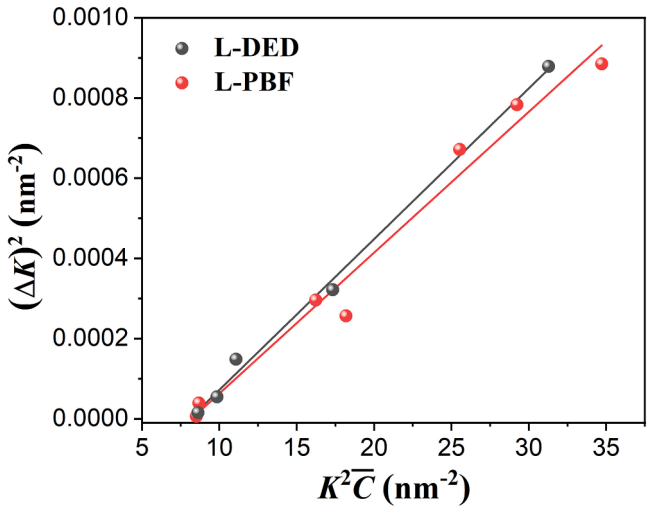

Fig. A.1. The modified Williamson-Hall plot for L-DED and L-PBF CoCrFeMnNi HEAs.

5. Conclusion

CoCrFeMnNi HEAs are fabricated by two additive manufacturing techniques, i.e., L-DED and L-PBF, which feature different temperature gradients and cooling rates. The two types of AM CoCrFeMnNi samples exhibit different melt pool geometries and microstructures including crystallographic textures and solidification cell structures, leading to different mechanical properties and deformation mechanisms. The main conclusions are drawn as follows:

(1) Both L-DED and L-PBF CoCrFeMnNi HEAs show heterogeneous microstructures, including heterogeneous grain geometries, subgrain solidification cells, and dislocation structures. Pronounced chemical segregation associated with the solidification cells is formed in the L-DED samples, while a relatively uniform elemental distribution is developed in the L-PBF samples due to higher cooling rates. Moreover, the lower width-to-height ratio of melt pools in the L-DED samples facilitates the formation of a mixed crystallographic texture of <101>/<111> as opposed to <001> in the L-PBF samples with a higher width-to-height ratio of melt pools.

(2) The L-DED and L-PBF samples exhibit comparable yield strengths, despite the lower cooling rate and substantially larger solidification cells in the former sample. However, the L-DED samples show a better combination of tensile strength and ductility relative to the L-PBF samples. The improved mechanical properties of L-DED samples arise from their higher work hardening rates that are rooted in the <101>/<111> crystallographic texture, larger solidification cell sizes, and chemical heterogeneity across the solidification cells.

(3) Post-deformation analyses reveal that planar slip is prevalent during the initial plastic deformation of both the L-DED and L-PBF samples. With increased plastic deformation, the <101>/<111> crystallographic texture and resultant high flow stresses in the L-DED samples facilitates the activation of abundant deformation twins. In addition, the larger solidification cell sizes and associated chemical heterogeneity across the cells in the L-DED samples increase the dislocation storage capability, leading to the formation of microbands during plastic deformation. The enhanced plastic deformation capabilities in the L-DED samples give rise to more sustained strain-hardening and thus higher ductility compared to the L-PBF samples.

Declaration of Competing Interest

The authors declare that they have no known competing financial interests or personal relationships that could have appeared to influence the work reported in this paper.

Acknowledgements

W. Chen acknowledges the support from National Science Foundation (DMR-2004429) and UMass Amherst Faculty Startup Fund. Wei Chen acknowledges the support from National Science Foundation (DMR-1945380). T. Zhu acknowledges the support from National Science Foundation (DMR-1810720 and DMR-2004412). Y. Liu acknowledges the support from the Natural Science Foundation of Jiangsu Province (Grants No BK20220962) and the technical support from Jiangsu Key Laboratory of Advanced Micro & Nano Materials and Technology and the Materials Characterization Facility of Nanjing University of Science and Technology. Neutron diffraction work was carried out at the Spallation Neutron Source (SNS), which is the U.S. Department of Energy (DOE) user facility at the Oak Ridge National Laboratory, sponsored by the Scientific User Facilities Division, Office of Basic Energy Sciences.

Supplementary materials

Supplementary material associated with this article can be found, in the online version, at doi:10.1016/j.actamat.2023.118884.

Appendix A. Dislocation density calculation

The dislocation density was calculated by the modified Williamson-Hall (MWH) method [62] which quantifies the average sub-grain (crystallite) size D and the strain effects on peak broadening as follows:

$$(\Delta K)^2 = (0.9/D)^2 + \left(\pi A^2 b^2 \rho / 2\right)\left(K^2\overline{C}\right) + O\left(K^2\overline{C}\right)^2 \quad (13)$$

where $K = 1/d$, $\Delta K = -K(\Delta d/d)$, d is the interplanar spacing and Δd the FWHM of the diffraction peaks, b the magnitude of the Burgers vector, ρ the dislocation density, A the dislocation distribution parameter depending on the effective outer cut-off radius of dislocations and usually ranging from 1~2 [80] and O representing the non-interpreted high order terms of $K^2\overline{C}$. Considering the effect of strain anisotropy among different reflections, the (hkl) dependent average dislocation contrast factor $\overline{C}$, is given by:

$$\overline{C} = \overline{C}_{h00}\left(1 - qH^2\right) \quad (14)$$

where $H^2 = (h^2k^2 + k^2l^2 + h^2l^2)/(h^2 + k^2 + l^2)^2$, and $\overline{C}_{h00}$ is the average dislocation contrast factor for (h00) reflections and related to the dislocation

type and anisotropic elastic constants C_{11}, C_{12}, and C_{44}. The values of $C_{11} = 172.1$ GPa, $C_{12} = 107.5$ GPa and $C_{44} = 92$ GPa used for calculation are taken from reference [81]. q is a variable related to the fractions of screw and edge dislocations, which can be experimentally determined by the least square linear regression of $[(\Delta K)^2 - (0.9/D)^2]/K^2$ versus H^2. The MWH plots are presented in Fig. A.1 and the slope of the linear fitting of $(\Delta K)^2$ versus $K^2\overline{C}$ is directly proportional to the dislocation density.

Appendix B. Thermodynamic and First-principals Calculations

Thermodynamic calculation of solidification path and segregation were performed with Thermo-Calc software using TCHEA v2.0 HEA thermodynamic database. Solidification path and segregation were simulated using a Scheil-Gulliver model, assuming no diffusion in any solid phases, infinite diffusion in liquid phases, and equilibrium at the solid-liquid interface [82].

First-principles calculations with the exact muffin-tin orbital-coherent-potential approximation (EMTO—CPA) method was performed for the CoCrFeMnNi HEA. The EMTO [83] method uses optimized overlapping muffin-tin potential spheres to represent the exact one-electron potential [84]. The one-electron equations were solved iteratively with the scalar relativistic approximation and the soft-core method. The EMTO method can be combined with the CPA [85] to describe the random mixing of elements in HEAs. The Perdew-Burke-Ernzerhof generalized gradient approximation (PBE) [86] was used to approximate the exchange-correlation functional. The EMTO Green's function was calculated self-consistently for 16 complex energy points that distributed exponentially [87].

The generalized stacking fault energy (GSFE) was calculated as the excess total energy associated with the formation of a stacking fault in an ideal FCC lattice. The stacking fault was created by sliding the z-axis perpendicular to the successive (111) planes with a series of displacement $n\mathbf{b}_p$ ($\mathbf{b}_p = a<211>/6$ and n is taken as 0.1) in the supercell. To eliminate the interactions between stacking fault with its periodic images, a supercell model of 9 FCC (111) layers was used [87]. The k-point mesh was carefully tested for convergence, and the $12 \times 24 \times 3$ mesh was used in all calculations to achieve an accuracy of 10^{-6} Ry/site. For each sliding step as $0.1\mathbf{b}_p$, the interlayer distances corresponding to the stacking fault layer were optimized [88], while the other interlayer distances were fixed at the equilibrium state.

References

[1] B. Cantor, I.T.H. Chang, P. Knight, A.J.B. Vincent, Microstructural development in equiatomic multicomponent alloys, Mater. Sci. Eng. A 375-377 (2004) 213–218.
[2] Z. Li, K.G. Pradeep, Y. Deng, D. Raabe, C.C. Tasan, Metastable high-entropy dual-phase alloys overcome the strength–ductility trade-off, Nature 534 (7606) (2016) 227–230.
[3] Z. Lei, X. Liu, Y. Wu, H. Wang, S. Jiang, S. Wang, X. Hui, Y. Wu, B. Gault, P. Kontis, D. Raabe, L. Gu, Q. Zhang, H. Chen, H. Wang, J. Liu, K. An, Q. Zeng, T.-.G. Nieh, Z. Lu, Enhanced strength and ductility in a high-entropy alloy via ordered oxygen complexes, Nature 563 (7732) (2018) 546–550.
[4] Y. Zhang, T.T. Zuo, Z. Tang, M.C. Gao, K.A. Dahmen, P.K. Liaw, Z.P. Lu, Microstructures and properties of high-entropy alloys, Prog. Mater. Sci. 61 (2014) 1–93.
[5] Q. Ding, Y. Zhang, X. Chen, X. Fu, D. Chen, S. Chen, L. Gu, F. Wei, H. Bei, Y. Gao, M. Wen, J. Li, Z. Zhang, T. Zhu, R.O. Ritchie, Q. Yu, Tuning element distribution, structure and properties by composition in high-entropy alloys, Nature 574 (7777) (2019) 223–227.
[6] P.D. Jablonski, J.J. Licavoli, M.C. Gao, J.A. Hawk, Manufacturing of high entropy alloys, JOM 67 (10) (2015) 2278–2287.
[7] Y.M. Wang, T. Voisin, J.T. McKeown, J. Ye, N.P. Calta, Z. Li, Z. Zeng, Y. Zhang, W. Chen, T.T. Roehling, R.T. Ott, M.K. Santala, Philip J. Depond, M.J. Matthews, A. V. Hamza, T. Zhu, Additively manufactured hierarchical stainless steels with high strength and ductility, Nat. Mater 17 (1) (2018) 63–71.
[8] T. Voisin, J.-.B. Forien, A. Perron, S. Aubry, N. Bertin, A. Samanta, A. Baker, Y. M. Wang, New insights on cellular structures strengthening mechanisms and thermal stability of an austenitic stainless steel fabricated by laser powder-bed-fusion, Acta Mater 203 (2021) 116476.
[9] Z.G. Zhu, Q.B. Nguyen, F.L. Ng, X.H. An, X.Z. Liao, P.K. Liaw, S.M.L. Nai, J. Wei, Hierarchical microstructure and strengthening mechanisms of a CoCrFeNiMn high entropy alloy additively manufactured by selective laser melting, Scripta Mater 154 (2018) 20–24.
[10] Q. Liu, H. Wu, M.J. Paul, P. He, Z. Peng, B. Gludovatz, J.J. Kruzic, C.H. Wang, X. Li, Machine-learning assisted laser powder bed fusion process optimization for AlSi10Mg: new microstructure description indices and fracture mechanisms, Acta Mater 201 (2020) 316–328.
[11] E.T. Furton, A.E. Wilson-Heid, A.M. Beese, Effect of stress triaxiality and penny-shaped pores on tensile properties of laser powder bed fusion Ti-6Al-4V, Addit. Manuf. 48 (2021), 102414.
[12] Y. Chew, G.J. Bi, Z.G. Zhu, F.L. Ng, F. Weng, S.B. Liu, S.M.L. Nai, B.Y. Lee, Microstructure and enhanced strength of laser aided additive manufactured CoCrFeNiMn high entropy alloy, Mater. Sci. Eng. A 744 (2019) 137–144.
[13] T.H. Becker, P. Kumar, U. Ramamurty, Fracture and fatigue in additively manufactured metals, Acta Mater 219 (2021), 117240.
[14] D. Kong, C. Dong, S. Wei, X. Ni, L. Zhang, R. Li, L. Wang, C. Man, X. Li, About metastable cellular structure in additively manufactured austenitic stainless steels, Addit. Manuf 38 (2021), 101804.
[15] D. Herzog, V. Seyda, E. Wycisk, C. Emmelmann, Additive manufacturing of metals, Acta Mater 117 (2016) 371–392.
[16] T. DebRoy, T. Mukherjee, J.O. Milewski, J.W. Elmer, B. Ribic, J.J. Blecher, W. Zhang, Scientific, technological and economic issues in metal printing and their solutions, Nat Mater 18 (10) (2019) 1026–1032.
[17] H.L. Wei, H.K.D.H. Bhadeshia, S.A. David, T. DebRoy, Harnessing the scientific synergy of welding and additive manufacturing, Sci. Technol. Weld. Joi. 24 (5) (2019) 361–366.
[18] S. Guan, D. Wan, K. Solberg, F. Berto, T. Welo, T.M. Yue, K.C. Chan, Additive manufacturing of fine-grained and dislocation-populated CrMnFeCoNi high entropy alloy by laser engineered net shaping, Mater. Sci. Eng. A 761 (2019), 138056.
[19] T. Voisin, J.-.B. Forien, A. Perron, S. Aubry, N. Bertin, A. Samanta, A. Baker, Y. M. Wang, New insights on cellular structures strengthening mechanisms and thermal stability of an austenitic stainless steel fabricated by laser powder-bed-fusion, Acta Mater 203 (2021), 116476.
[20] M. Zięłala, T. Durejko, M. Polański, I. Kunce, T. Płociński, W. Zieliński, M. Łazińska, W. Stępniowski, T. Czujko, K.J. Kurzydłowski, Z. Bojar, The microstructure, mechanical properties and corrosion resistance of 316L stainless steel fabricated using laser engineered net shaping, Mater. Sci. Eng. A 677 (2016) 1–10.
[21] B. Gludovatz, A. Hohenwarter, D. Catoor, E.H. Chang, E.P. George, R.O. Ritchie, A fracture-resistant high-entropy alloy for cryogenic applications, Science 345 (6201) (2014) 1153–1158.
[22] G. Laplanche, A. Kostka, O.M. Horst, G. Eggeler, E.P. George, Microstructure evolution and critical stress for twinning in the CrMnFeCoNi high-entropy alloy, Acta Mater 118 (2016) 152–163.
[23] K. An, VDRIVE-data reduction and interactive visualization software for event mode neutron diffraction, Report No. ORNL-TM-2012-621, ORNL (2012).
[24] K.V. Yang, Y. Shi, F. Palm, X. Wu, P. Rometsch, Columnar to equiaxed transition in Al-Mg(-*Sc*)-Zr alloys produced by selective laser melting, Scripta Mater 145 (2018) 113–117.
[25] T. Wang, Y.Y. Zhu, S.Q. Zhang, H.B. Tang, H.M. Wang, Grain morphology evolution behavior of titanium alloy components during laser melting deposition additive manufacturing, J. Alloys Compd. 632 (2015) 505–513.
[26] W. Chen, T. Voisin, Y. Zhang, J.B. Florien, C.M. Spadaccini, D.L. McDowell, T. Zhu, Y.M. Wang, Microscale residual stresses in additively manufactured stainless steel, Nat Commun 10 (1) (2019) 4338.
[27] Y.-.T. Lin, X. An, Z. Zhu, M.L.S. Nai, C.-.W. Tsai, H.-.W. Yen, Effect of cell wall on hydrogen response in CoCrFeMnNi high-entropy alloy additively manufactured by selective laser melting, J. Alloys Compd. 925 (2022), 166735.
[28] Z. Li, Y. Cui, W. Yan, D. Zhang, Y. Fang, Y. Chen, Q. Yu, G. Wang, H. Ouyang, C. Fan, Q. Guo, D.-.B. Xiong, S. Jin, G. Sha, N. Ghoniem, Z. Zhang, Y.M. Wang, Enhanced Strengthening and Hardening Via Self-Stabilized Dislocation Network in Additively Manufactured Metals 50, Mater. Today, 2021, pp. 79–88.
[29] M.S. Pham, C. Solenthaler, K.G.F. Janssens, S.R. Holdsworth, Dislocation structure evolution and its effects on cyclic deformation response of AISI 316L stainless steel, Mater. Sci. Eng. A 528 (7) (2011) 3261–3269.
[30] M.J. Starink, S.C. Wang, A model for the yield strength of overaged Al–Zn–Mg–Cu alloys, Acta Mater 51 (17) (2003) 5131–5150.
[31] Z. Li, B. He, Q. Guo, Strengthening and hardening mechanisms of additively manufactured stainless steels: the role of cell sizes, Scripta Mater 177 (2020) 17–21.
[32] K. Ming, X. Bi, J. Wang, Strength and ductility of CrFeCoNiMo alloy with hierarchical microstructures, Int. J. Plast. 113 (2019) 255–268.
[33] Z. Wang, H. Bei, I. Baker, Microband induced plasticity and the temperature dependence of the mechanical properties of a carbon-doped FeNiMnAlCr high entropy alloy, Mater. Charact. 139 (2018) 373–381.

[34] D.L. Foley, S.H. Huang, E. Anber, L. Shanahan, Y. Shen, A.C. Lang, C.M. Barr, D. Spearot, L. Lamberson, M.L. Taheri, Simultaneous twinning and microband formation under dynamic compression in a high entropy alloy with a complex energetic landscape, Acta Mater 200 (2020) 1–11.
[35] Y. Cao, S. Ni, X. Liao, M. Song, Y. Zhu, Structural evolutions of metallic materials processed by severe plastic deformation, Mater. Sci. Eng. R 133 (2018) 1–59.
[36] H.W. Zhang, X. Huang, N. Hansen, Evolution of microstructural parameters and flow stresses toward limits in nickel deformed to ultra-high strains, Acta Mater 56 (19) (2008) 5451–5465.
[37] Y. Liu, Y. Cao, Q. Mao, H. Zhou, Y. Zhao, W. Jiang, Y. Liu, J.T. Wang, Z. You, Y. Zhu, Critical microstructures and defects in heterostructured materials and their effects on mechanical properties, Acta Mater 189 (2020) 129–144.
[38] M.N. Hasan, Y.F. Liu, X.H. An, J. Gu, M. Song, Y. Cao, Y.S. Li, Y.T. Zhu, X.Z. Liao, Simultaneously enhancing strength and ductility of a high-entropy alloy via gradient hierarchical microstructures, Int. J. Plast. 123 (2019) 178–195.
[39] L. Liu, Q. Ding, Y. Zhong, J. Zou, J. Wu, Y.-L. Chiu, J. Li, Z. Zhang, Q. Yu, Z. Shen, Dislocation network in additive manufactured steel breaks strength–ductility trade-off, Mater. Today 21 (4) (2018) 354–361.
[40] H. Beladi, I.B. Timokhina, Y. Estrin, J. Kim, B.C. De Cooman, S.K. Kim, Orientation dependence of twinning and strain hardening behaviour of a high manganese twinning induced plasticity steel with polycrystalline structure, Acta Mater 59 (20) (2011) 7787–7799.
[41] X. Wang, J.A. Muñiz-Lerma, M.Attarian Shandiz, O. Sanchez-Mata, M. Brochu, Crystallographic-orientation-dependent tensile behaviours of stainless steel 316L fabricated by laser powder bed fusion, Mater. Sci. Eng. A 766 (2019) 138395.
[42] D. Caillard, J.-L. Martin, Thermal Activated Mechanisms in Crystal Plasticity, 2003. Pergamon, Amsterdam.
[43] Z. Yin, X. Yang, X. Ma, J. Moering, J. Yang, Y. Gong, Y. Zhu, X. Zhu, Strength and ductility of gradient structured copper obtained by surface mechanical attrition treatment, Mater. Design 105 (2016) 89–95.
[44] E.P. George, W.A. Curtin, C.C. Tasan, High entropy alloys: a focused review of mechanical properties and deformation mechanisms, Acta Mater 188 (2020) 435–474.
[45] Z. An, S. Mao, T. Yang, C.T. Liu, B. Zhang, E. Ma, H. Zhou, Z. Zhang, L. Wang, X. Han, Spinodal-modulated solid solution delivers a strong and ductile refractory high-entropy alloy, Mater. Horiz. 8 (3) (2021) 948–955.
[46] J. Ren, Y. Zhang, D. Zhao, Y. Chen, S. Guan, Y. Liu, L. Liu, S. Peng, F. Kong, J. D. Poplawsky, G. Gao, T. Voisin, K. An, Y.M. Wang, K.Y. Xie, T. Zhu, W. Chen, Strong yet ductile nanolamellar high-entropy alloys by additive manufacturing, Nature 608 (2022) 62–68.
[47] W. Jiang, S. Yuan, Y. Cao, Y. Zhang, Y. Zhao, Mechanical properties and deformation mechanisms of a Ni2Co1Fe1V0.5Mo0.2 medium-entropy alloy at elevated temperatures, Acta Mater 213 (2021) 116982.
[48] L. Lu, T. Zhu, Y. Shen, M. Dao, K. Lu, S. Suresh, Stress relaxation and the structure size-dependence of plastic deformation in nanotwinned copper, Acta Mater 57 (17) (2009) 5165–5173.
[49] S.M. Chowdhury, D.L. Chen, S.D. Bhole, E. Powidajko, D.C. Weckman, Y. Zhou, Microstructure and mechanical properties of fiber-laser-welded and diode-laser-welded AZ31 magnesium alloy, Metall. Mater. Trans. A 42 (7) (2011) 1974–1989.
[50] K.M. Bertsch, G. Meric de Bellefon, B. Kuehl, D.J. Thoma, Origin of dislocation structures in an additively manufactured austenitic stainless steel 316L, Acta Mater 199 (2020) 19–33.
[51] H. Wang, Z.G. Zhu, H. Chen, A.G. Wang, J.Q. Liu, H.W. Liu, R.K. Zheng, S.M.L. Nai, S. Primig, S.S. Babu, S.P. Ringer, X.Z. Liao, Effect of cyclic rapid thermal loadings on the microstructural evolution of a CrMnFeCoNi high-entropy alloy manufactured by selective laser melting, Acta Mater 196 (2020) 609–625.
[52] A.J. Birnbaum, J.C. Steuben, E.J. Barrick, A.P. Iliopoulos, J.G. Michopoulos, Intrinsic strain aging, Σ3 boundaries, and origins of cellular substructure in additively manufactured 316L, Addit. Manuf. 29 (2019), 100784.
[53] M.-.S. Pham, B. Dovgyy, P.A. Hooper, C.M. Gourlay, A. Piglione, The role of side-branching in microstructure development in laser powder-bed fusion, Nat. Commun. 11 (1) (2020) 749.
[54] T. DebRoy, H.L. Wei, J.S. Zuback, T. Mukherjee, J.W. Elmer, J.O. Milewski, A. M. Beese, A. Wilson-Heid, A. De, W. Zhang, Additive manufacturing of metallic components – process, structure and properties, Prog. Mater. Sci. 92 (2018) 112–224.
[55] L. Thijs, M.L. Montero Sistiaga, R. Wauthle, Q. Xie, J.-.P. Kruth, J. Van Humbeeck, Strong morphological and crystallographic texture and resulting yield strength anisotropy in selective laser melted tantalum, Acta Mater 61 (12) (2013) 4657–4668.
[56] Z. Sun, X. Tan, S.B. Tor, C.K. Chua, Simultaneously enhanced strength and ductility for 3D-printed stainless steel 316L by selective laser melting, NPG Asia Mater 10 (4) (2018) 127–136.
[57] K. Ma, H. Wen, T. Hu, T.D. Topping, D. Isheim, D.N. Seidman, E.J. Lavernia, J. M. Schoenung, Mechanical behavior and strengthening mechanisms in ultrafine grain precipitation-strengthened aluminum alloy, Acta Mater 62 (2014) 141–155.
[58] R.W. Armstrong, Engineering science aspects of the Hall–Petch relation, Acta Mech. 225 (4) (2014) 1013–1028.
[59] F. Otto, A. Dlouhý, C. Somsen, H. Bei, G. Eggeler, E.P. George, The influences of temperature and microstructure on the tensile properties of a CoCrFeMnNi high-entropy alloy, Acta Mater 61 (15) (2013) 5743–5755.
[60] N. Hansen, Boundary strengthening in undeformed and deformed polycrystals, Mater. Sci. Eng. A 409 (1–2) (2005) 39–45.
[61] J.E. Bailey, P.B. Hirsch, The dislocation distribution, flow stress, and stored energy in cold-worked polycrystalline silver, Philos. Mag. 5 (53) (1960) 485–497.
[62] G.K. Williamson, W.H. Hall, X-ray line broadening from filed aluminium and wolfram, Acta Metall 1 (1) (1953) 22–31.
[63] P. Rodriguez, Grain size dependence of the activation parameters for plastic deformation: influence of crystal structure, slip system, and rate-controlling dislocation mechanism, Metall. Mater. Trans. A 35 (9) (2004) 2697–2705.
[64] Q. Yang, Q. Sun, W. Yang, Q. Hao, X. Wang, B. Zhang, Correlation between microstructure evolution and mechanical response in a moderately low stacking-fault-energy austenitic Fe–Mn–Si–Al alloy during low-cycle fatigue deformation, Mater. Sci. Eng. A 824 (2021) 141766.
[65] R. Zhang, S. Zhao, J. Ding, Y. Chong, T. Jia, C. Ophus, M. Asta, R.O. Ritchie, A. M. Minor, Short-range order and its impact on the CrCoNi medium-entropy alloy, Nature 581 (7808) (2020) 283–287.
[66] A.J. Zaddach, C. Niu, C.C. Koch, D.L. Irving, Mechanical properties and stacking fault energies of NiFeCrCoMn high-entropy alloy, JOM 65 (12) (2013) 1780–1789.
[67] X. Wang, R.R. De Vecchis, C. Li, H. Zhang, X. Hu, S. Sridar, Y. Wang, W. Chen, W. Xiong, Design metastability in high-entropy alloys by tailoring unstable fault energies, Sci. Adv. 8 (36) (2022) eabo7333.
[68] K.-.T. Chen, T.-.J. Wei, G.-.C. Li, M.-.Y. Chen, Y.-.S. Chen, S.-.W. Chang, H.-.W. Yen, C.-.S. Chen, Mechanical properties and deformation mechanisms in CoCrFeMnNi high entropy alloys: a molecular dynamics study, Mater. Chem. Phys. 271 (2021), 124912.
[69] S. Lee, M.J. Duarte, M. Feuerbacher, R. Soler, C. Kirchlechner, C.H. Liebscher, S. H. Oh, G. Dehm, Dislocation plasticity in FeCoCrMnNi high-entropy alloy: quantitative insights from in situ transmission electron microscopy deformation, Mater. Res. Lett. 8 (6) (2020) 216–224.
[70] S. Curtze, V.T. Kuokkala, Dependence of tensile deformation behavior of TWIP steels on stacking fault energy, temperature and strain rate, Acta Mater 58 (15) (2010) 5129–5141.
[71] I. Gutierrez-Urrutia, D. Raabe, Microbanding mechanism in an Fe–Mn–C high-Mn twinning-induced plasticity steel, Scripta Mater 69 (1) (2013) 53–56.
[72] Z. Zhang, Z. Jiang, Y. Xie, S.L.I. Chan, J. Liang, J. Wang, Multiple deformation mechanisms induced by pre-twinning in CoCrFeNi high entropy alloy, Scripta Mater 207 (2022) 114266.
[73] I.A. Ovid'ko, R.Z. Valiev, Y.T. Zhu, Review on superior strength and enhanced ductility of metallic nanomaterials, Prog. Mater. Sci. 94 (2018) 462–540.
[74] I. Gutierrez-Urrutia, S. Zaefferer, D. Raabe, The effect of grain size and grain orientation on deformation twinning in a Fe–22wt.% Mn–0.6wt.% C TWIP steel, Mater. Sci. Eng. A 527 (15) (2010) 3552–3560.
[75] S.M. Copley, B.H. Kear, The dependence of the width of a dissociated dislocation on dislocation velocity, Acta Metall 16 (2) (1968) 227–231.
[76] I. Karaman, H. Sehitoglu, K. Gall, Y.I. Chumlyakov, H.J. Maier, Deformation of single crystal Hadfield steel by twinning and slip, Acta Mater 48 (6) (2000) 1345–1359.
[77] I.V. Kireeva, Y.I. Chumlyakov, Z.V. Pobedennaya, I.V. Kuksgausen, I. Karaman, Orientation dependence of twinning in single crystalline CoCrFeMnNi high-entropy alloy, Mater. Sci. Eng. A 705 (2017) 176–181.
[78] I.V. Kireeva, Y.I. Chumlyakov, Z.V. Pobedennaya, A.V. Vyrodova, I. Karaman, Twinning in [001]-oriented single crystals of CoCrFeMnNi high-entropy alloy at tensile deformation, Mater. Sci. Eng. A 713 (2018) 253–259.
[79] I. Karaman, H. Sehitoglu, Y.I. Chumlyakov, H.J. Maier, I.V. Kireeva, Extrinsic stacking faults and twinning in hadfield manganese steel single crystals, Scripta Mater 44 (2) (2001) 337–343.
[80] F. HajyAkbary, J. Sietsma, A.J. Böttger, M.J. Santofimia, An improved X-ray diffraction analysis method to characterize dislocation density in lath martensitic structures, Mater. Sci. Eng. A 639 (2015) 208–218.
[81] M. Naeem, H. He, S. Harjo, T. Kawasaki, F. Zhang, B. Wang, S. Lan, Z. Wu, Y. Wu, Z. Lu, C.T. Liu, X.-.L. Wang, Extremely high dislocation density and deformation pathway of CrMnFeCoNi high entropy alloy at ultralow temperature, Scripta Mater 188 (2020) 21–25.
[82] N.E. Uzan, R. Shneck, O. Yeheskel, N. Frage, High-temperature mechanical properties of AlSi10Mg specimens fabricated by additive manufacturing using selective laser melting technologies (AM-SLM), Addit. Manuf. 24 (2018) 257–263.
[83] L. Vitos, I.A. Abrikosov, B. Johansson, Anisotropic lattice distortions in random alloys from first-principles theory, Phys. Rev. Lett. 87 (15) (2001), 156401.
[84] O.K. Andersen, C. Arcangeli, R.W. Tank, T. Saha-Dasgupta, G. Krier, O. Jepsen, I. Dasgupta, Third-Generation TB-LMTO, MRS Proc. 491 (1997) 3.
[85] B.L. Gyorffy, Coherent-Potential Approximation for a Nonoverlapping-Muffin-Tin-Potential Model of Random Substitutional Alloys, Phys. Rev. B 5 (1972) 2382–2384.
[86] W. Li, S. Lu, Q.-.M. Hu, S.K. Kwon, B. Johansson, L. Vitos, Generalized stacking fault energies of alloys, J. Phys. 26 (26) (2014), 265005.
[87] H. Huang, X. Li, Z. Dong, W. Li, S. Huang, D. Meng, X. Lai, T. Liu, S. Zhu, L. Vitos, Critical stress for twinning nucleation in CrCoNi-based medium and high entropy alloys, Acta Mater 149 (2018) 388–396.
[88] L.-.Y. Tian, R. Lizárraga, H. Larsson, E. Holmström, L. Vitos, A first principles study of the stacking fault energies for fcc Co-based binary alloys, Acta Mater 136 (2017) 215–223.